Microstructural Evolution and Ductile-to-Brittle Transition in a Low-Carbon MnCrMoNiCu Heavy Plate Steel

DONGSHENG LIU, MI LUO, BINGGUI CHENG, RUI CAO, and JIANHONG CHEN

Low carbon MnCrMoNiCu alloyed steels are typically used to produce highly ductile thick plates for offshore structures and bulk shipbuilding. The current study revealed how microscopic factors affect the toughness and the occurrence of cleavage fracture of the steel. In this regard, a series of thermal treatments was performed on the test steel by employing a thermomechanical simulator. These involved reheating samples at different temperatures (1168 K to 1623 K (895 °C to 1350 °C)) producing different prior austenite grain sizes, followed by a continuous cooling transformation process. The Charpy V notch (CVN) toughness was determined, and the effect of the austenite grain size on the ductile–brittle transition-temperatures of the steel was investigated. The microstructural evolution of the austenite grain sizes was studied, fracture features were characterized, the critical event for cleavage fracture was identified, and the local cleavage fracture stress σ_f was calculated. The CVN toughness and σ_f were maximized in the steel which was reheated at 1273 K (1000 °C) and containing refined lathlike bainite.

I. INTRODUCTION

A structural steel should not be used at temperatures lower than the ductile-to-brittle transition temperature (DBTT), at which the steel loses most of its toughness and fractures in the brittle cleavage mode.[1–3] In the course of cleavage fracture, transgranular cracking takes place along the typical cleavage of the $\{100\}_\alpha$ plane. The fracture stress σ_f is an intrinsic mechanical property pertaining to the cleavage fracture and is insensitive to temperature. The increase in σ_f can lower the DBTT, as demonstrated by the Yoffee diagram.[1–3]

The engineering significance in studying the variations in σ_f with microstructural factors and the scientific fascination in clarifying micromechanism of the cleavage fracture in high-strength steels have stimulated substantial research works[2,4–8] The microstructural units controlling the σ_f were different for different steels: ferrite grains in polygonal ferrite + pearlite steels, bainitic, or martensitic packets in quenched and tempered steels, or the prior austenite grains in the as-quenched steels.[2,6,8] A Griffith form can be employed to link the σ_f and microstructural factors, i.e., grain size or packet size, and the effective energy of the fracture surface, γ_p. Hanamura et al.[2] found that γ_p could be quantified as 7.7, 34.6, and 150.9 J/m² for ferrite + pearlite, tempered martensite, or the as-quenched martensite, respectively, in a JIS-SM490 steel. γ_p of 233.3 J/m² was reported for a high-strength bainitic steel.[6] The local cleavage fracture stress σ_f decreases as the packets size increases, showing a linear dependence on the inverse square root of the size.[7,8] The decrease of σ_f made cleavage fracture easier, increased the DBTT, and worsened the toughness in the lower shelf region.

The effect of microstructural variants, including prior austenite grain size, bainitic/martensitic packet size, distribution of martensite–austenite (MA) constituents, and the density of high-angle grain boundaries (HAGBs), on the DBTT of the steels has been revealed.[9–16] It has been believed that the presence of MA constituents is deleterious, as it increases DBTT.[9,16] The prior austenite grain boundaries,[2,6] or the boundaries that separate different colonies of the martensitic or bainitic microstructure, could be HAGBs. These boundaries inhibit the propagation of cleavage cracks.[10,11] Furthermore, it has been suggested that Bain unit

DONGSHENG LIU, MI LUO, and BINGGUI CHENG are with the Institute of Research of Iron and Steel, Jiangsu Shagang Group Co., Ltd, Jinfeng Town, Zhangjiagang, Jiangsu Province 215625, P.R. China. Contact e-mail: dongshengl@hotmail.com RUI CAO and JIANHONG CHEN are with the State Key Laboratory of Gansu Advanced Processing and Recycling of Non-ferrous Metallic Metals and Key Laboratory of Non-ferrous Metal Alloys of the Ministry of Education, Lanzhou University of Technology, Lanzhou 730050, P.R. China.

boundaries[12–14] could prevent cleavage crack propagation in martensitic steels. In addition, the HAGBs within bainitic packets could deflect the crack-propagation path[15] or form fine tear ridges on the fracture surface and provide additional resistance, but is not the decisive factor determining crack propagation.[6] Based on these previous studies, it is believed that DBTT would decrease with the increasing fraction of HAGBs.

The variations in the microstructure and mechanical properties of highly ductile low-carbon steel plates with high yield strength (YS) greater than 690 MPa have been the subject of extensive investigation.[17–25] The delivered plates are heat treated by the conventional quenching and tempering process. The as-quenched microstructures can vary, being lath martensite (LM), lath bainite (LB), or granular bainite (GB) depending on the chemical composition, thickness of the plate, location across the thickness, and the quenching process. Dhua et al.[18] demonstrated that the YS, the ultimate tensile strength (UTS), and Charpy V Notch (CVN) properties of the specimens with LM microstructures were much superior to those with the GB microstructure in HSLA-100 steels. LB is also a reasonably well-accepted as-quenched microstructure as demonstrated by a recent study on an 80-mm-thick plate of YS 690 MPa.[23] It was found that the CVN energy in the quarter thickness with LB was approximately three times as high as that in the core of the plate, where GB was dominant. This is attributed to the LB microstructure that comprises a higher density of HAGBs and hence smaller effective grain sizes compared to those of the GB microstructure. The formation of GB with coarse MA constituents in the steel is in turn due to the limited cooling rates achievable in the core of the heavy plates even during quenching. This should be mitigated in the quenched and tempered plate. A recent study by You et al.[22] demonstrated that LB associated with fine MA constituents was achieved even during slow cooling at 1 K/s (1 °C/s) by increasing the austenitizing temperature to 1000 °C for an HSLA-100 steel. The CVN impact toughness of the steel was thus maximized. However, further studies on the variation in DBTT with the austenitizing temperature and corresponding cleavage fracture behavior may be required as part of this study.

Welding is a critical process in high-strength steels.[26–31] The microstructure in the heat-affected zone (HAZ) of the base metal would be altered during thermal cycles, when the matrix phases transform into austenite during heating, which in turn retransform into microstructures such as martensite or bainite depending on the cooling rate (or heat input) during cooling. The austenite grain size in the coarse-grained heat-affected zone (CGHAZ) may be 10 times higher than that in a fine-grained HAZ (FGHAZ)[26,31]; as a result, the

toughness of the CGHAZ would be reduced. A recent study[23] showed that the Charpy V impact toughness was dramatically reduced in the simulated unaltered CGHAZ. The changes in the toughness of the base metal and CGHAZ were associated with the occurrence of cleavage fracture. The local cleavage fracture stress σ_f is considered as the resistance offered by the weakest microstructural component to the propagation of a cleavage crack, i.e., it is a characteristic of steel that decisively controls cleavage fracture and toughness.[5] It is therefore essential to study the microstructural factors that can maximize the fracture stress σ_f, and thereby lower the DBTT, in developing advanced highly ductile HSLA steels. Systematic investigations on the micromechanism of the cleavage fracture behavior in high-strength steels (YS greater than 690 MPa grade) are still inadequate and scarce.[6,7]

In the current study, the micromechanism governing the DBTT of an industrially produced low-carbon MnCrMoNiCu plate steel with YS greater than 690 MPa was studied. The effect of microstructural variation on the fracture behavior was studied based on the principles of the micromechanism of the cleavage fracture of the metal.[5]

II. EXPERIMENTAL PROCEDURES

The chemical composition of the steel is shown in Table I. The steel was produced by an integrated industrial production process including steelmaking using a basic oxygen furnace, ladle furnace, Ruhrstahl-Hereus degassing system, and continuous casting, resulting in slabs of thickness 320 mm. An 80 mm-thick plate was rolled from one of the slabs with a 5-m-wide plate mill. After reheating at 1473 K (1200 °C) for 20 minutes, the slab was subjected to rough rolling, with a total reduction ratio of 50 pct, and finish rolling, again with a total reduction ratio of 50 pct, in the austenite recrystallization and non-recrystallization regions, respectively.[23] Specimens of dimensions 11 mm × 1 mm × 75 mm were taken from the quarter thickness section for the subsequent heat treatments. The length direction was perpendicular to the rolling direction.

Thermal simulations were performed using a thermomechanical simulator. A Pt-10 pct Rh thermocouple was spot welded in the middle along the length of the specimens for recording the temperature. Each specimen was heated at 5 K/s (5 °C/s) up to a predetermined temperature of 1168 K, 1273 K, 1473 K, or 1623 K (895 °C, 1000 °C, 1200 °C, or 1350 °C), held there for 5 min, and then continuously cooled at 5 K/s (5 °C/s) down to 773 K (500 °C) followed by a continuous cooling transformation (CCT) at 2.5 K/s (2.5 °C/s) to room temperature.

Table I. Chemical Composition of the Experimental Steel (Weight Percent)

C	Si	Mn	P	S	Cu	Ni	Cr	Mo	Al	Nb	Ti
0.07	0.23	1.06	0.008	0.001	1.25	1.74	0.59	0.485	0.036	0.043	0.019

The as-quenched samples were cross sectioned, and the plane coinciding with the thermocouple position was ground and polished by the conventional technique. Saturated aqueous picric acid was used to reveal the austenite grain boundaries at 338 ± 5 K (65 ± 5 °C). A nital reagent composed of 4 pct nitric acid in denatured ethanol was used to reveal the transformed microstructures. The austenite grain size or bainitic/martensitic packet size was measured as the average value of the two diameters perpendicular to each other using an optical microscope. The individual packets were characterized based on the morphology or growth orientation of ferrite laths. The transformed microstructures at room temperature were further observed with a scanning electron microscope (SEM). Electron backscatter diffraction (EBSD) analysis (resolution: 0.1 μm) was performed by employing a field emission SEM equipped with an EBSD camera. The data were then interpreted using the HKL technology Channel 5 software. These samples were also subjected to Vickers hardness testing using a 10 kg load. A more detailed metallographic examination was performed on the selected specimens using a TEM equipped with energy dispersive spectroscopy (EDS) attachment. The thin foils for TEM observations (at 200 kV) were prepared in a twin-jet electrolytic apparatus using a solution containing 5 vol pct perchloric acid and 95 vol pct ethanol.

For *in situ* observations on the microstructure evolution during the CCT, a sample was sectioned from the plate and machined into a disk (3.8 mm diameter × 3 mm height), mirror polished, and set into a high-purity alumina crucible (4.5 mm inner diameter × 5 mm height). The microstructure during heating was observed with a confocal scanning laser microscope (CSLM).[32] The sample and crucible were placed into a gold image furnace and heated at 5 K/s (5 °C/s) to the desired temperatures in high-purity argon to prevent any oxidation. The microstructural changes with the temperature and time were observed and recorded for final analysis.

Standard CVN specimens (10 mm × 10 mm × 55 mm) were prepared with the V notch parallel to the direction of thickness at the position of spot-welded thermocouple. The impact energy was measured at room temperature, 253 K, 213 K, 188 K, 168 K, or 77 K (RT, − 20 °C, − 60, °C − 85, °C − 105, °C or − 196 °C) by employing a 450-J instrumented pendulum impact tester with a tup striker of radius 2 mm. The load and the absorbed energy pertaining to the displacement curves measured by the impact tester were recorded for further analysis. The determination of dynamic load at the yielding point P_y will be shown in a subsequent section on the results of the instrumented Charpy V impact tests. The derivation of the global dynamic yield strength σ_{dy} from the measured P_y was based on Server's study.[33] The constraint factor C is defined as

$$C = 2M/k(W - a)^2 \qquad [1]$$

where M is bending moment per unit thickness (B), k the shear yield strength, a the notch depth, W the specimen width. Assuming the Tresca yield criterion ($\sigma_{dy} = 2k$),

$$\sigma_{dy} = 4M/C(W - a)^2 \qquad [2]$$

Substituting for the applied three point bending moment M at the general yield (for a span-to-width ratio of 4),

$$\sigma_{dy} = 4P_y W/CB(W - a)^2 \qquad [3]$$

Taking the constrain factor C as 1.336 for the notch specimen,

$$\sigma_{dy} = 2.99P_y W/B(W - a)^2 \qquad [4]$$

The fracture surfaces of the failed Charpy V specimens were observed in detail using SEM. The relative microscopic parameters were measured for analyzing the micromechanism of the fracture. The fracture surface may consist of (1) an original notch; (2) a stretch zone (SZW), which is actually produced by blunting the original notch root and is characterized by a smooth formless pattern; (3) an area of ductile fracture with a fine dimple pattern, in which a fibrous crack length (SCL) could be measured; and (4) a cleavage cracking zone (CCZ) that shows several cleavage facets with river pattern trips on them. The fracture distance X_f is the distance from the site of cleavage crack initiation to the blunted notch tip or fibrous crack. The cleavage-initiation site was located by tracing back the river pattern strips to their origins, and X_f was measured. The SZW, SCL, and CCZ present an integrated cracking process. The details of the methodology to measure the SZW, SCL, or X_f have been documented in the literature.[5,8] To find the cracks retained in the failed sample, the cross sections perpendicular to both the fracture surface and the length direction of the V notch were polished, etched by the nital solution, and examined under the optical microscope and SEM.

III. RESULTS

A. *Prior Austenite Microstructure at Austenitizing Temperature*

Prior austenite grain size (PAGS), which determines the type of microstructure, packet size, or block size, or the density of HAGBs, increased as the austenitizing temperature was increased. At least 110 austenite grain sizes were measured for each austenitizing condition. The sizes of the coarsest prior austenite grains or the mean PAGS varied with the austenitizing temperature, being 30.7 or 15.8 μm at 1168 K (895 °C), 62.3 or 22.0 μm at 1273 K (1000 °C), and 122.3 or 59.0 μm at 1473 K (1200 °C). A dramatic increase in the mean grain size to 233.1 μm associated with the coarsest grain of 533.8 μm was observed when the reheating temperature was increased to 1623 K (1350 °C) (listed in Table II). Figure 1 shows the original austenite grains observed in the specimens with the increasing austenitizing temperature.

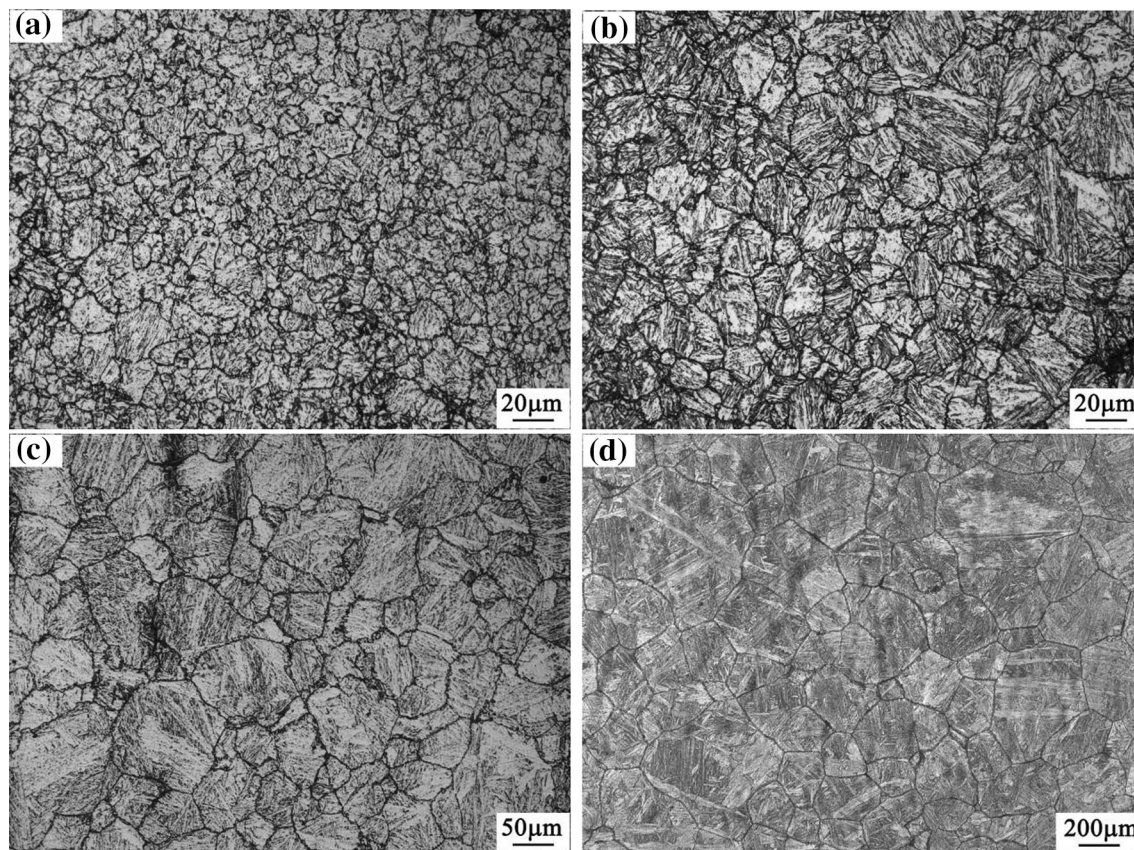| T_{RH} K (°C)	Max Size of Prior Austenite (μm)	Max Size of Packet (μm)	Fraction of HAGB	Hardness (HV)	DBTT K (°C)
1168 (895)	30.7	29.4	63	305	202 (− 71)
1273 (1000)	62.3	31.6	72	334	179 (− 94)
1473 (1200)	122.3	59.4	72	339	217 (− 56)
1623 (1350)	533.8	201.6	86	333	221 (− 52)

Fig. 1—Austenite grains (picric acid solution etching) of the specimen austenitized at (*a*) 1168 K (895 °C), (*b*) 1273 K (1000 °C), (*c*) 1473 K (1200 °C), and (*d*) 1623 K (1350 °C).

B. *In situ Observation on Austenite-to-Bainite/Martensite Transformation*

Surface relief is typically associated with the formation of bainitic/martensitic ferrite during the austenite-to-bainite/martensite transformation. This has been successfully observed using a high-temperature laser scanning confocal microscope in previous studies on low-carbon steels.[34–36] The current study observed the microstructural evolution in the specimens austenitized at 1273 K, 1473 K, and 1623 K (1000 °C, 1200 °C, and 1350 °C) by using a similar technique. Figure 2 shows bainite nucleation and growth in the specimen austenitized at 1273 K (1000 °C). Bainitic transformation by grain-boundary nucleation is observed, and the growth of bainitic ferrite is inhibited on the opposite side of the grain boundary, as indicated by the black arrows in Figures 2(b) and (c). Subsequently, the simultaneous

formation of bainitic ferrite in different orientations is observed during continuous cooling (Figure 2(d)). In the specimen austenitized at 1473 K (1200 °C), bainitic/martensitic ferrite mainly nucleated on the prior austenite grain boundaries, and the growth was again inhibited on the opposite boundaries (Figures 3(b) through (d)). Subsequently, nucleation on the sides of the newly created ferrite grains was observed; and the growth of ferrite can also cause impingement between the grains (Figures 3(e) through (g)). It can be seen that the circled coarse austenite grain was fragmented, resulting in a few packets due to the impingement (Figure 3(h)). In the specimen austenitized at 1623 K (1350 °C), the austenite grains were much coarser; both the grain-boundary (indicated by black arrows) and intragranular nucleation (indicated by white arrows) transformation mechanisms were observed
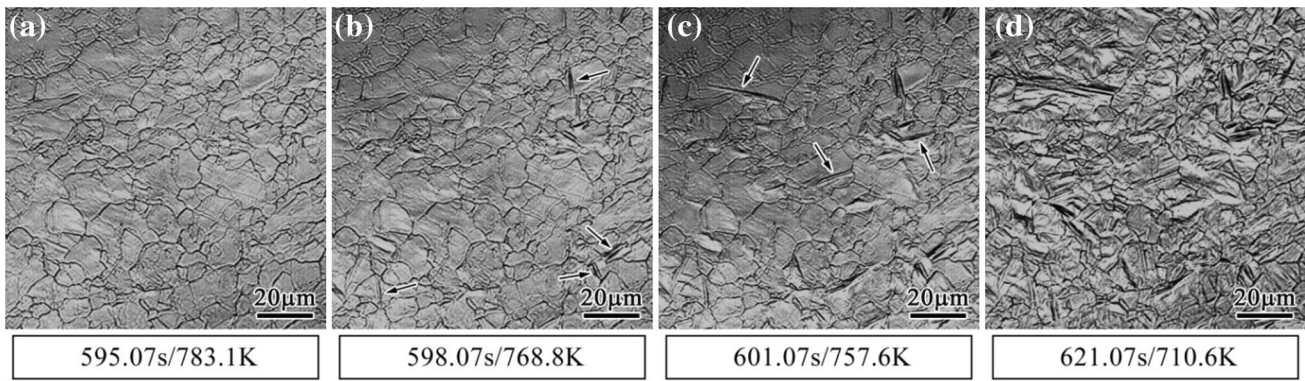
Fig. 2—Snapshots of CSLM images showing the microstructural evolution of the specimen austenitized at 1273 K (1000 °C): (*a*) prior austenite; (*b*), (*c*) ferrite laths nucleated on austenite grain boundaries and the inhibition of their growth at the opposite boundaries; and (*d*) formation of lathlike bainite.
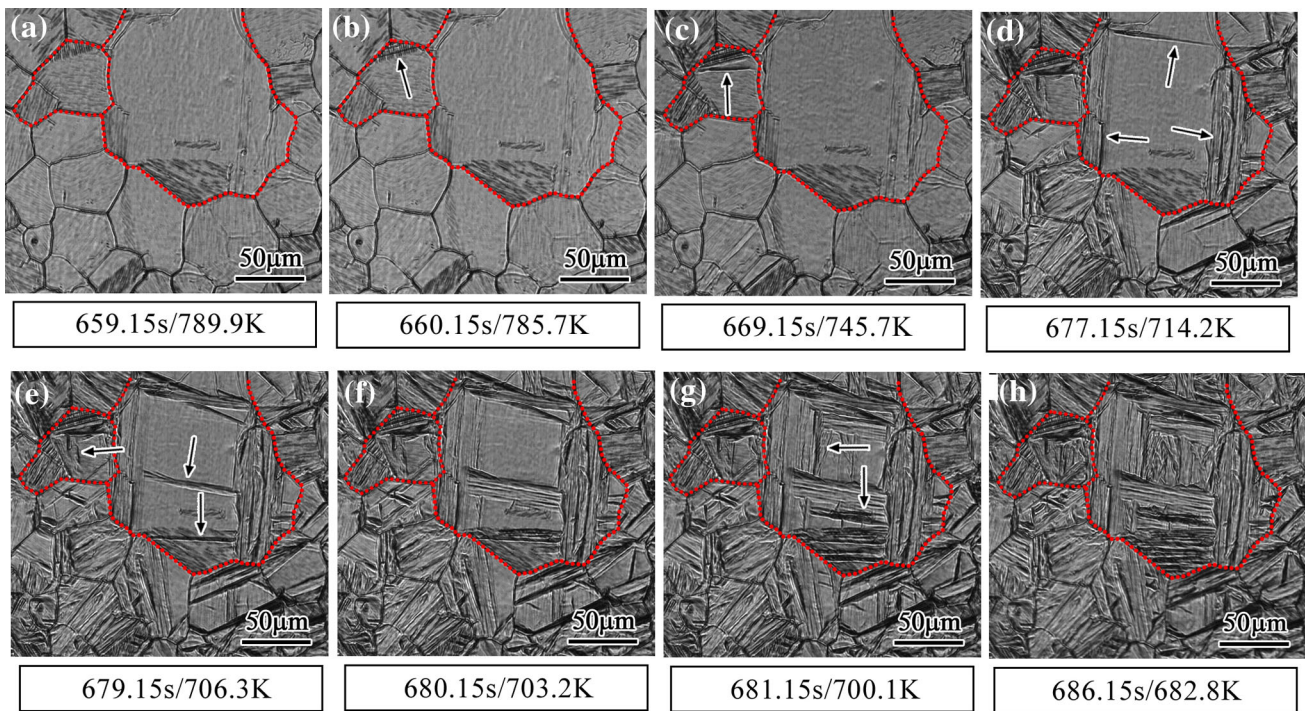

Fig. 3—Snapshots of CSLM images showing the microstructural evolution of the specimen austenitized at 1473 K (1200 °C): (*a*) prior austenite; (*b*) through (*d*) ferrite laths nucleated on austenite grain boundaries and the inhibition of their growth at the opposite grain boundaries; (*e*) through (*g*) parallel ferrite laths nucleated on the sides of a newly created ferrite lath and the inhibition of their growth in the prior austenite grains due to impingement; and (*h*) the large prior austenite grain was fragmented by several packets.

(Figure 4(b)). Subsequently, ferrites nucleate sympathetically on the surface of the primary ferrite associated with the impingement events. Based on two-dimensional observations, therefore, grain-boundary nucleation was found to be the most common mechanism at the start of the transformation. The impingement of ferritic laths is absent when the PAGS is small (Figure 2); however, it occurs when the austenite grain size becomes larger (Figures 3 and 4). Furthermore, the current study found that intragranular nucleation of bainite is stimulated in completion with the grain-boundary nucleation mechanism when the austenite grains are substantially coarsened. It is addressed that some of the observed

intragranular nucleations may involve martensite/bainite that nucleated at the austenite grain boundaries existing at a certain depth from the specimen surface, before they grew and appeared at the surface.

C. Resultant Microstructures After Continuous Cooling Transformation

The change in microstructure with austenitizing temperature during the transformation was qualitatively or quantitatively characterized. Figure 5 shows the optical morphologies in the specimens austenitized at 1168 K, 1273 K, 1473 K, or 1623 K (895 °C, 1000 °C,
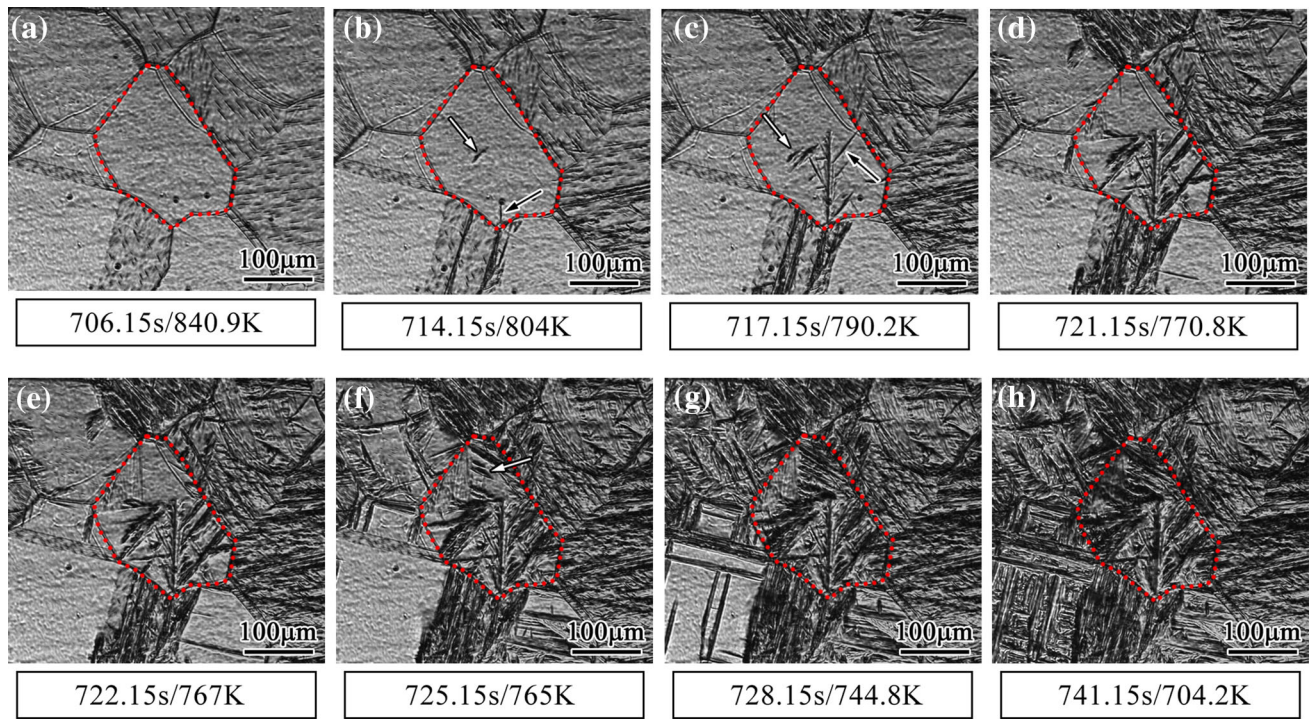
Fig. 4—Snapshots of CSLM images showing the microstructural evolution of the specimen austenitized at 1623 K (1350 °C): (*a*) austenite microstructure prior to phase transformation; (*b*) intragranular nucleation (white arrow) and grain-boundary nucleation (black arrow); (*c*) through (*f*) continuing intragranular nucleation, and impingement of grain-boundary-nucleated ferrite laths; and (*g*), (*h*) growth of parallel ferrite laths nucleated on the sides of a newly formed ferrite lath.
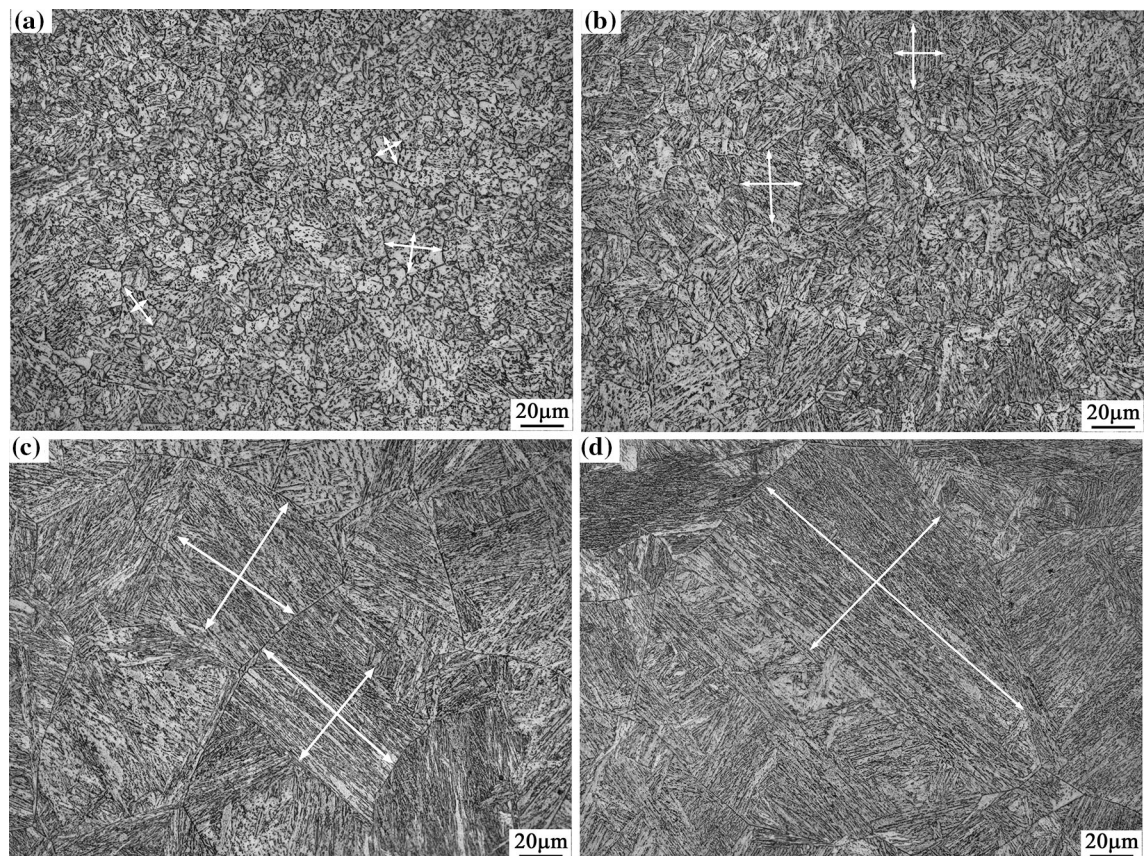

Fig. 5—Morphologies as observed under an optical microscope (after 4 pct nital etching) and measurement of packet size for the specimens austenitized at (*a*) 1168 K (895 °C), (*b*) 1273 K (1000 °C), (*c*) 1473 K (1200 °C), and (*d*) 1623 K (1350 °C).
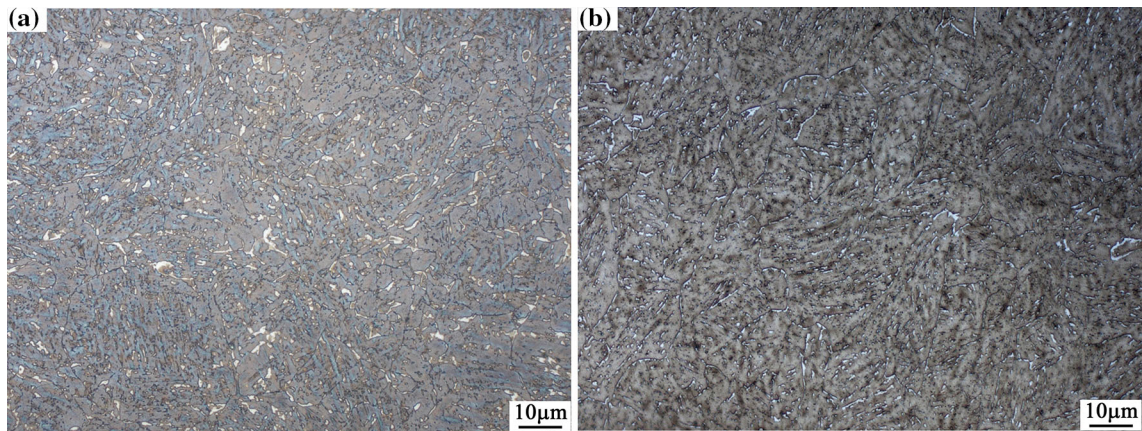
Fig. 6—Morphologies as observed under an optical microscope (LePera regent) for the specimens austenitized at (*a*) 1168 K (895 °C) and (*b*) 1273 K (1000 °C) showing a white phase corresponding to the MA constituents.
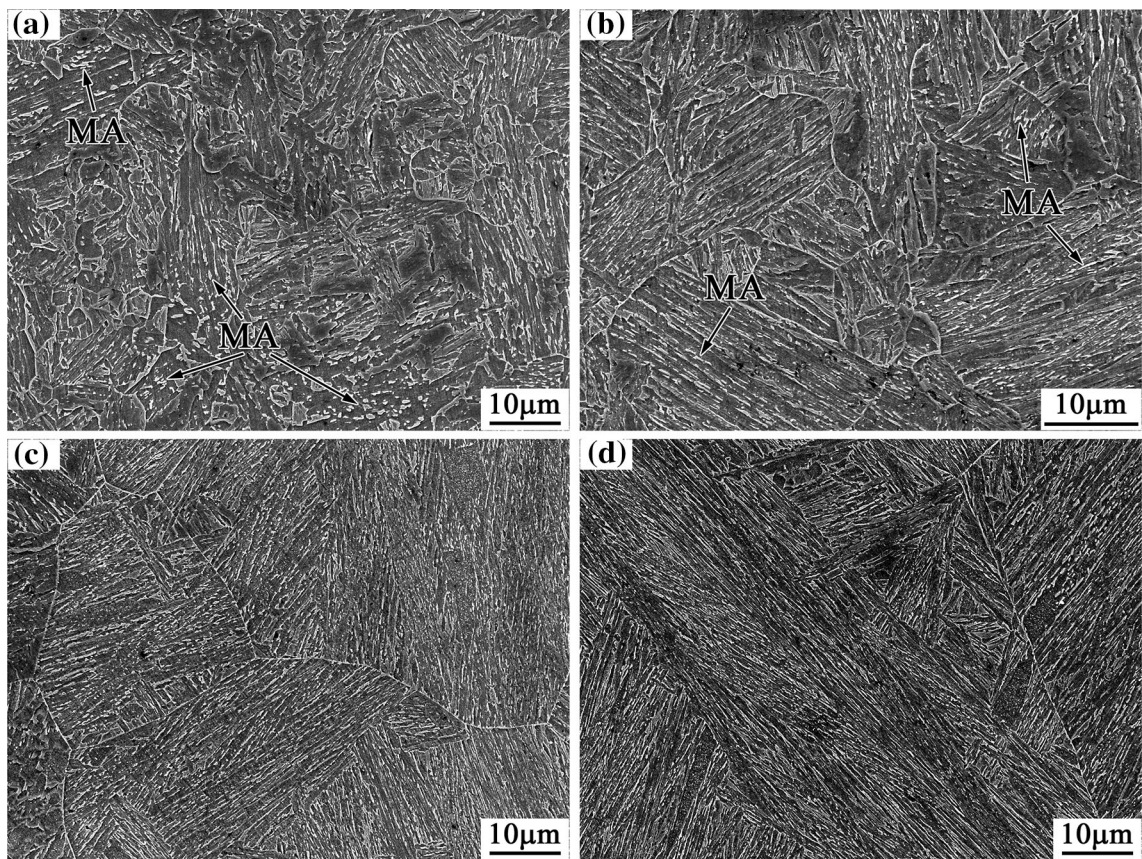

Fig. 7—SEM images of the (4 pct nital etched) specimens austenitized at (*a*) 1168 K (895 °C), (*b*) 1273 K (1000 °C), (*c*) 1473 K (1200 °C), and (*d*) 1623 K (1350 °C).

1200 °C, or 1350 °C), respectively. The method of measuring packet sizes by using the optical microscope is also indicated. At least 160 delineated packet sizes were measured for each austenitizing condition. Figure 6 shows the decreasing quantity of the MA constituents as the austenitizing temperature is increased. The SEM morphologies of the microstructures are shown in Figure 7. The microstructure in the specimen austenitized at 1168 K (895 °C) is mainly a

GB–LB mixture, with 3.97 pct of the MA constituents. The microstructure in the specimen austenitized at 1273 K (1000 °C) mainly comprises LB and refined MA constituents (1.20 pct) (Figure 6). The microstructure of the specimen austenitized at 1473 K or 1623 K (1200 °C or 1350 °C) is dominated by LM + LB. The maximum packet sizes increased with the increasing austenitizing temperature, being 29.4, 31.6, 59.4, and 201.6 μm for 1168 K, 1273 K, 1473 K, and 1623 K

Table III. Microparameters for Cleavage Fracture at 77 K ($-$196 °C)

T_{RH} K (°C)	a_f (µm)	P_f (kN)	P_y (kN)	P_f/P_y	σ_{dy} (MPa)	X_f (µm)	σ_f (MPa)	ε_{pc}	T_c	$Q_c(\sigma_f/\sigma_{dy})$	γ_p (J/m^2)
1168 (895)	32.8	10.10	30.54	0.331	1427	68.0	2102	0.014	0.81	1.47	210
1273 (1000)	33.0	16.70	32.49	0.514	1518	295.0	2868	0.004	1.21	1.89	393
1473 (1200)	45.1	7.90	32.00	0.247	1454	50.0	1908	0.004	0.22	1.27	237
1623 (1350)	55.9	6.60	31.50	0.216	1425	80.0	1853	0.001	0.69	1.30	278

a_f cleavage facet size around the crack-initiation site, σ_{dy} dynamic yield strength, σ_f local cleavage fracture stress, ε_{pc} fracture strain, T_C critical stress triaxiality, Q_C critical stress intensification factor, γ_p effective surface energy, P_f fracture load, and X_f critical distance of cleavage.
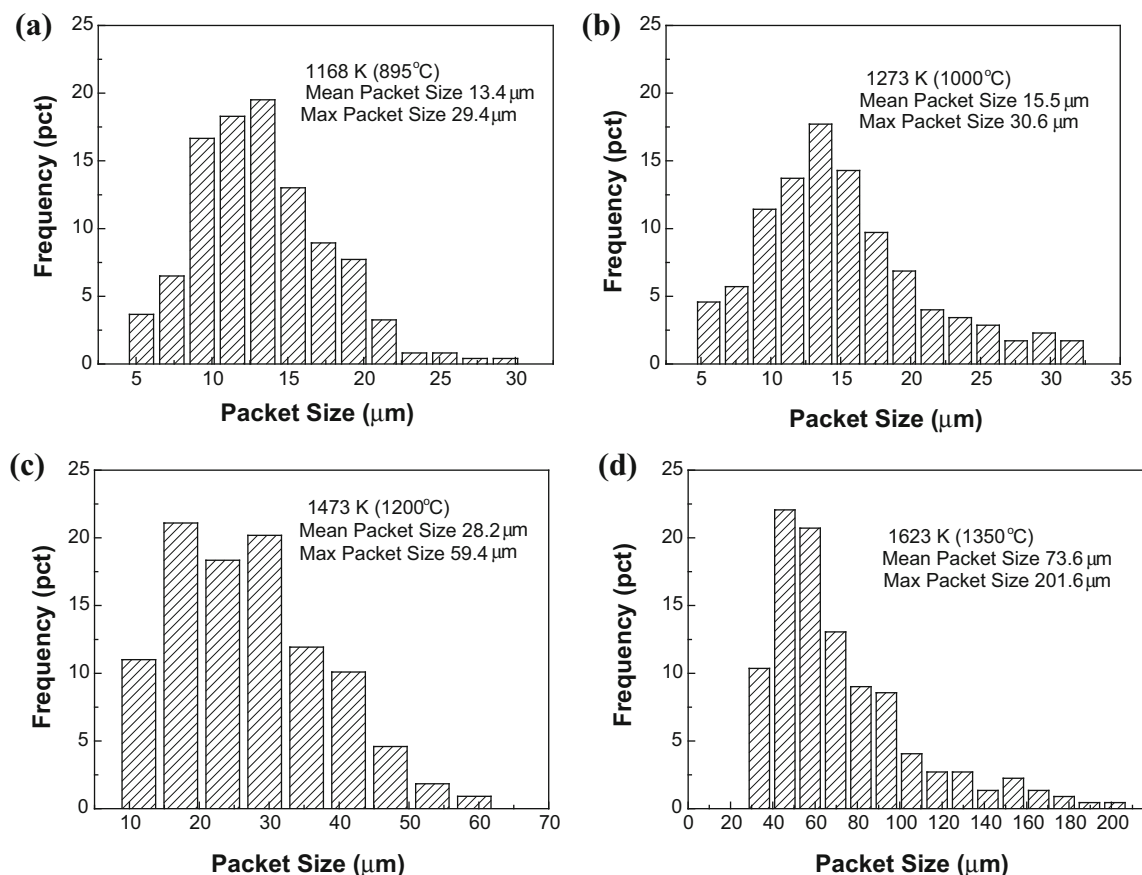

Fig. 8—Bainite (along with some martensite in (c, d)) packets of the specimens austenitized at (a) 1168 K (895 °C), (b) 1273 K (1000 °C), (c) 1473 K (1200 °C), and (d) 1623 K (1350 °C).

(895 °C, 1000 °C, 1200 °C, and 1350 °C), respectively (listed in Table II). The corresponding frequency distributions of the packet sizes in all the conditions are shown in Figure 8. The variations of both PAGS and the resultant bainitic/martensitic packet size vs the austenitizing temperature are shown in Figure 9. One can see that the packet size decreases as the PAGS decreases. The maximum packet sizes of the GB microstructure are approximately equal to those of the prior austenite grains. The coarsest packet sizes of the LM microstructure are approximately 0.38 to 0.49 times those of the coarsest prior austenite grains (Table III). This is roughly consistent with the theoretical analysis.[37]

Figure 10 shows the TEM images of the specimens austenitized at 1168 K, 1273 K, or 1623 K (895 °C, 1000 °C or 1350 °C, respectively). Laths of bainitic

ferrite are the major matrix microstructure in the specimen austenitized at 1168 K (895 °C) with fine-grained prior austenite. These laths are associated with islands of MA (pointed by arrows) that form GB, as shown in Figure 10(b). Both the laths and the MA constituents in the specimen austenitized at 1273 K (1000 °C) are finer than those of the specimen austenitized at 1168 K (895 °C) (Figures 10(c) and (d)). In the specimen austenitized at 1623 K (°C), which is coarse-grained, dislocated martensite laths were observed as the matrix, and some of the laths experienced significant autotempering during the cooling process, as shown in Figures 10(e) and (f). A similar autotempering phenomenon was also observed by Thompson et al.[38] in the study of a HSLA-80 steel during continuous cooling processes.
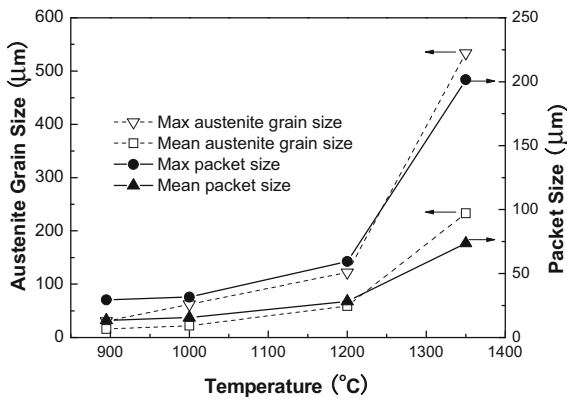
Fig. 9—Changes in prior austenite grain size and transformed bainitic (or martensitic) packet size with austenitizing temperature.

Figure 11 presents the EBSD maps showing the HAGBs (greater than 15 deg) in the specimens austenitized at different temperatures with different PAGSs. It can be seen that the fraction of HAGBs increases as the PAGS increases, as shown in Figure 12(a). The majority of the HAGBs are characterized by misorientations greater than 35 deg, as shown in Figure 12(b). The boundaries of prior austenite grains, the boundaries of the packets, and some interlath boundaries within packets parallel to each other are characterized by the high-angle misorientations. The increased fraction of HAGBs could be attributed to the formation of LM and LB microstructures, in which the misorientations of the interlath boundaries typically involve high angles.

D. Charpy V Impact Testing and the Curves of Load–Energy vs Displacement

Based on the CVN testing at different temperatures, the DBTT was determined for each austenitizing condition. Figure 13 presents the ductile-to-brittle transition curves measured under all the conditions. The DBTT, which is defined as the temperature corresponding to the average value of the upper and lower shelf energies, was characterized as 202 K, 179 K, 217 K, and 221 K (-71 °C, -94 °C, -56, and -52 °C) for the austenitizing at 1168 K, 1273 K, 1473 K, and 1623 K (895 °C, 1000 °C, 1200 °C, and 1350 °C), respectively. It indicates that the optimal low-temperature toughness is not achieved in the specimen austenitized at 1168 K (895 °C) with the finest prior austenite grains. This is attributed to the presence of a GB microstructure with coarse MA constituents. Rather, the toughness is maximized in the specimen austenitized at 1273 K (1000 °C) with LB, where the packet sizes are similar to those of the specimen with GB.

The characteristics of the fractures in the fully ductile upper-shelf region, transition region, and lower shelf region are reflected in the curves of the CVN impact load combined with the impact energy vs hammer displacement, as shown in Figure 14. At an impact loading P, a distribution of the principal stress σ_{yy} along the distance to the root of the V notch would be established if no cracking takes place.[5] In the upper

shelf region, the load P reaches and exceeds the yield load P_y, causing substantial plastic deformation and work hardening until final ductile rupture. The CVN energy includes both the crack-initiation energy and fibrous crack-propagation energy. A crack-initiation energy of around 50 J can be differentiated from the curves (Figures 14(a) and (b)). A 191-J crack-propagation energy can be measured in the specimen tested at 293 K (20 °C), and a 145-J-crack-propagation energy in the specimen tested at 188 K (-85 °C). The decreased propagation energy can be attributed to the decrease in plasticity as the test temperature is decreased (see the total displacement for Figures 14(a) and (b)). In the ductile-to-brittle transition region (Figure 14(c)), P reaches P_y, causing fibrous crack propagation and work hardening in the early stage, followed by a brittle cleavage crack; as a result, the total CVN absorbed energy is reduced. The earlier the cleavage crack is triggered, the lower is the CVN absorbed energy. In the lower shelf region, P_y and σ_{dy} are increased due to the decrease in test temperature; as a result, the applied stress σ_{yy} reaches the fracture stress σ_f before the fibrous crack propagation can take place, which triggers cleavage fracture without substantially preceding fibrous crack propagation, as is the case in the transition region (Figure 14(d)).

E. Fractographs of the Failed Charpy V Specimens

A fully ductile fracture with a dimple pattern was observed in the upper shelf region for each processing condition, as shown in Figure 15. The general mode of fracture on the upper shelf is ductile, caused by the extension of the microcracks formed by the primary voids (the dimples on the fracture surface) that nucleate and grow until impingement, resulting in coalescence and final rupture. In the investigated steel, most of the second-phase particles that initiated the dimples were identified as CaO, MgO, and CaS. With the decreasing impact test temperature (Figures 15(a) and (b)) and the increasing austenitizing temperature (increasing PAGS), the sizes of the dimples seem to decrease. The plasticity decreases as the temperature decreases. It also decreases with the increasing PAGS.[8] The decreases in the plasticity may lead to differences in the impact energy in the upper shelf region, shown in Figure 13.

Representative SEM fractographs of the CVN samples fractured in the ductile-to-brittle transition region are shown in Figure 16. The fracture surface consists of ductile (fibrous crack propagation) and brittle fracture regions. During the impact testing, a width of the SZW is formed by blunting the tip of the notch, and subsequently, a length of fibrous crack (SCL) is formed as a result of significant plastic deformation; brittle cleavage fracture is finally triggered. The microcrack parameters measured in the transition region are shown in Table IV. The ductile-to-brittle transition takes place in all the specimens between 213 K and 188 K (-60 to -85 °C), except for the sample austenitized at 1273 K (1000 °C), in which the ductile-to-brittle transition fractures were observed at 173 K (-100 °C) or lower. Here, the total absorbed energy (E_t) changes in the order
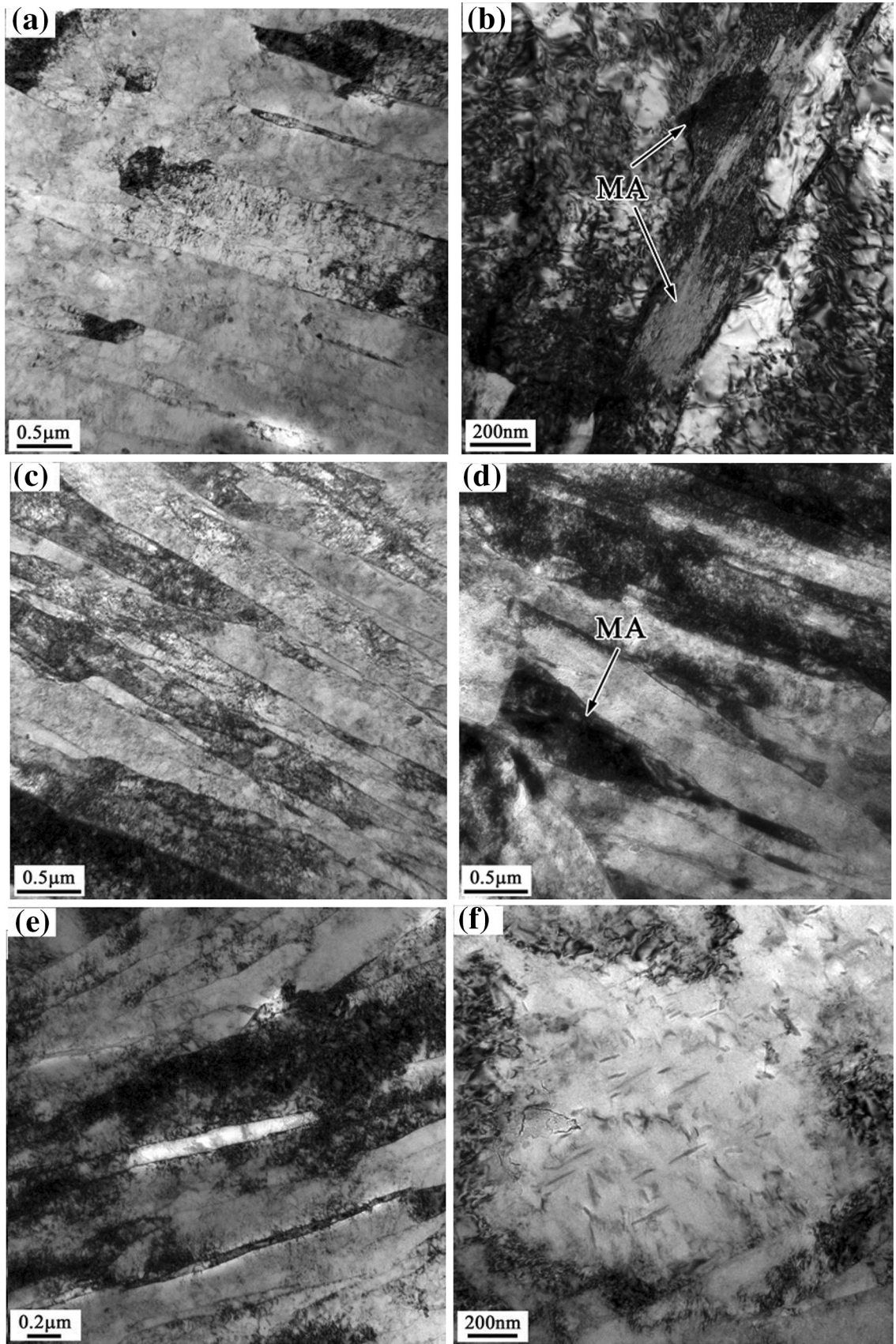
Fig. 10—Thin foil TEM images of the specimens austenitized at (*a*) and (*b*) 1168 K (895 °C), (*c*) and (*d*) 1273 K (1000 °C), and (*e*) and (*f*) 1623 K (1350 °C).
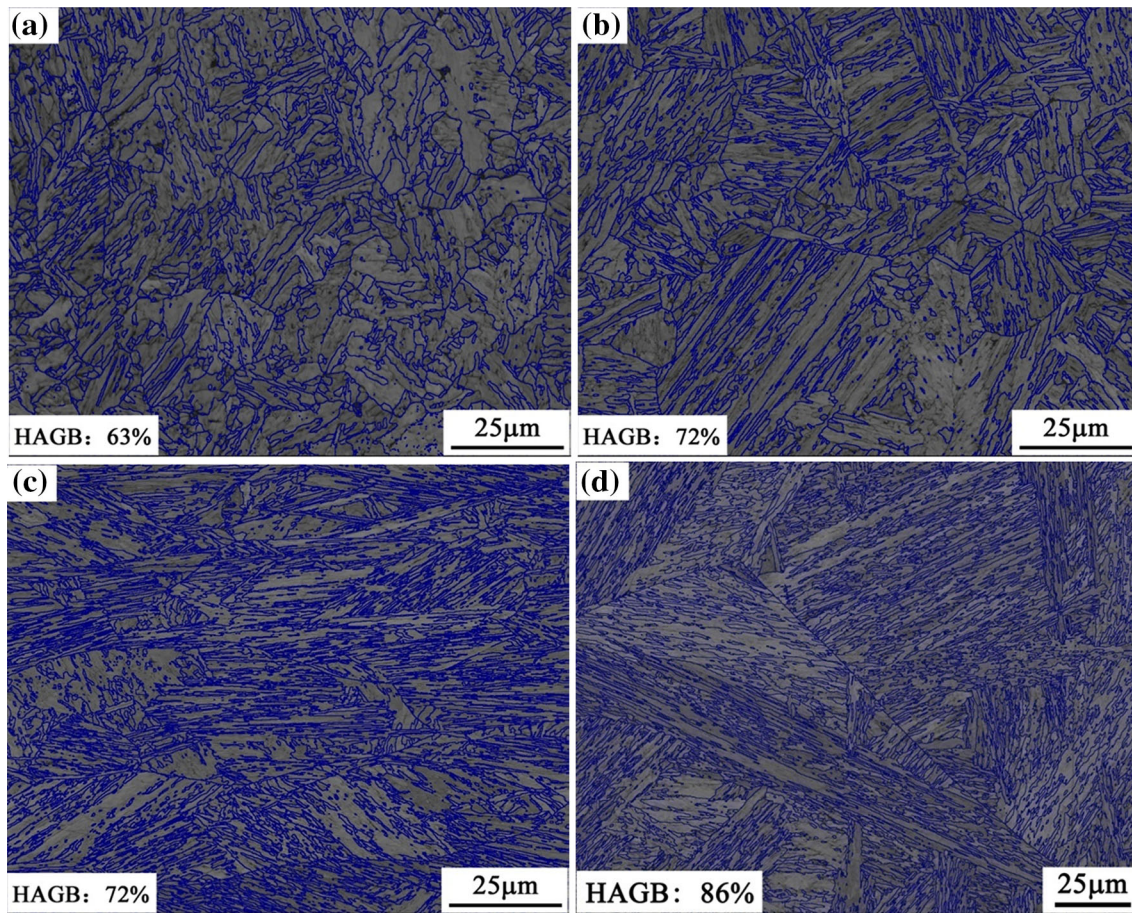
Fig. 11—EBSD maps of the specimens austenitized at (a) 1168 K (895 °C), (b) 1273 K (1000 °C), (c) 1473 K (1200 °C), and (d) 1623 K (1350 °C) (the thick lines are the grain boundaries with misorientations greater than 15 deg).
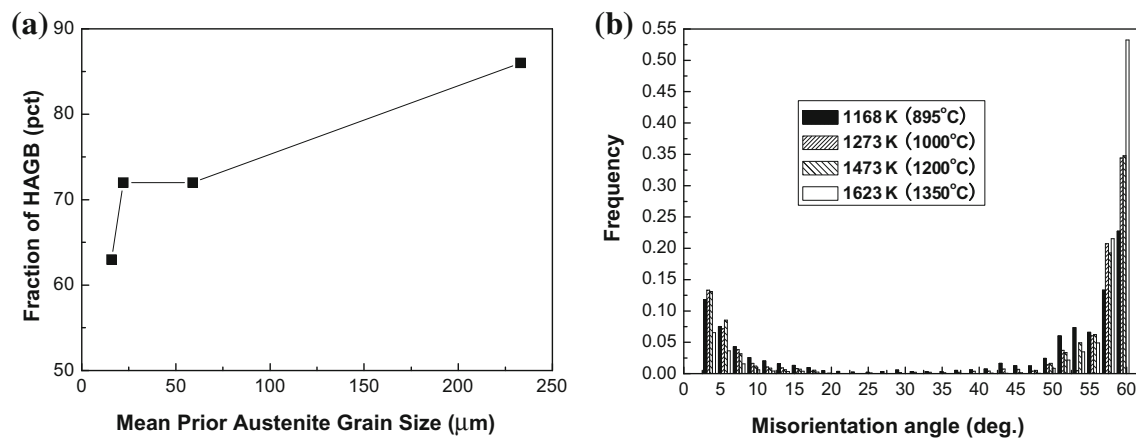

Fig. 12—(a) Fraction of HAGBs vs mean austenite grain size and (b) frequency distribution of grain-boundary misorientations for each austenitizing temperature.

of the width of fibrous crack propagation. The E_t during impact fracture increases as the sum of SZW and SCL increases.[8,39]

The fractographs of the specimens that failed in the brittle mode in the lower shelf region are displayed in Figure 17. A microcrack may be initiated from a second-phase particle, which then propagates across a bainite/martensite high-angle packet boundary, leading to final failure. The origins and pathways of the microcrack propagation are indicated by yellow arrows. The feature of the cleavage surface around the crack-initiation site can be linked with the microstructures under different conditions, i.e., the size of the cleavage fracture facet changes in the order consistent with the order of

packet sizes. The coarse tear ridges are of the packet boundaries. The fine parallel tear ridges within the cleavage facet can be attributed to the interlath boundaries with high misorientations.[6] Although the cleavage facet sizes corresponding to Figures 17(a) and (b) are similar to each other, the density of tear ridges in the former, with GB, is lower than that in the latter, with LB. The tear ridges made the cleavage facet shown in
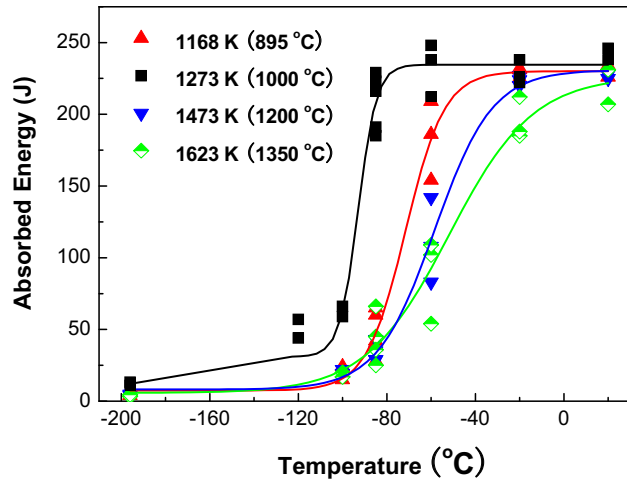

Fig. 13—Ductile-to-brittle transition curves of the specimens austenitized at the temperatures indicated.

Figure 17(b) are uneven compared to that shown in Figure 17(a). By identifying the crack-initiation site, the cleavage fracture distance X_f was measured (listed in Table III).

F. Critical Event for the Cleavage Fracture

The cleavage microcracking process is composed of (1) crack nucleation, (2) crack propagation across the particle–grain boundary, and (3) crack propagation across the grain–grain boundary.[11] It is essential to identify which one of the above three stages is the greatest difficulty, i.e., the critical event, in the formation of a cleavage crack. In low- to medium-strength steels with ferrite and pearlite, the propagation of a grain-sized crack into contiguous grains is the critical event for the cleavage fracture of notched specimens.[5] Figure 18 displays the cracks retained in the specimens with different microstructures. The retained cracks are constrained in a packet, and their further propagation is inhibited at the packet boundaries. The crack propagation in the GB grains seemed to be rather straight (Figure 18(a)), whereas secondary crack propagation took place in some LB grains (Figure 18(b) through (d)). The packet boundaries that inhibited further crack propagation were HAGBs —this was confirmed by orientation mapping using EBSD, as shown in Figure 19. The observations in the current study indicate that the critical event for cleavage fracture can be
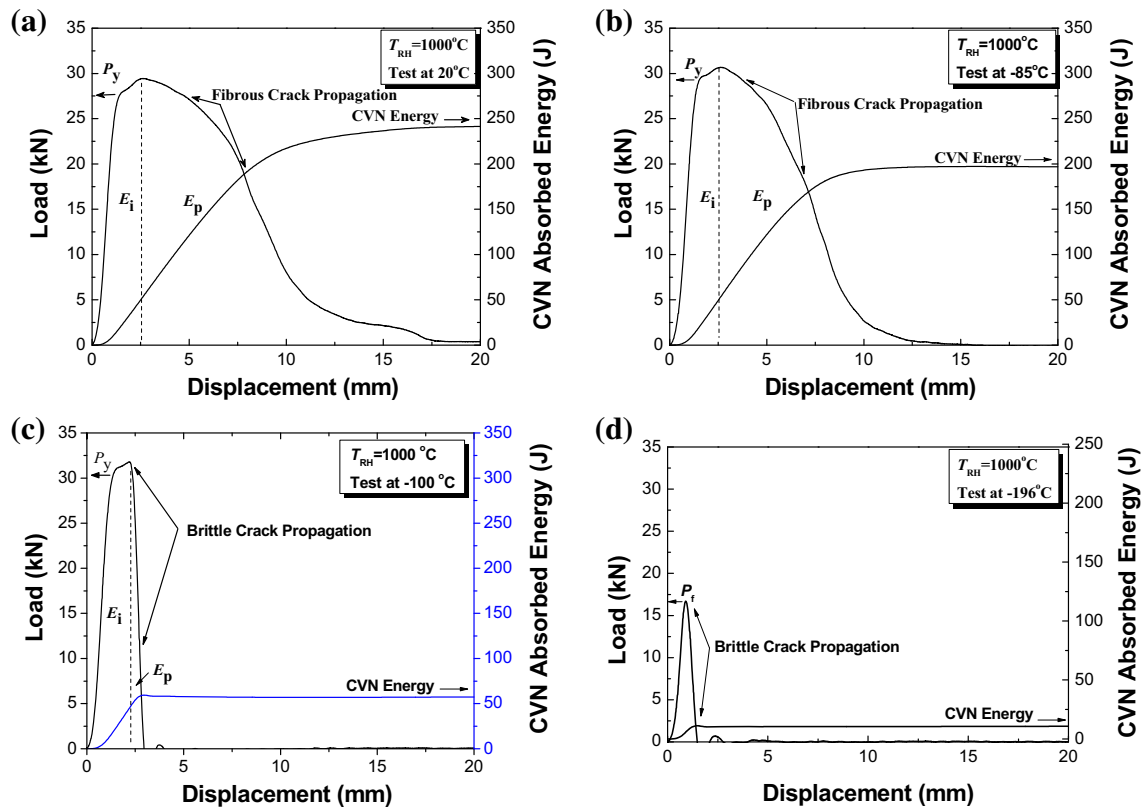

Fig. 14—Curves of load and Charpy impact energy (CVN) vs hammer displacement obtained from the instrumented impact tests for the specimens austenitized at 1273 K (1000 °C) and tested at (a) 293 K (20 °C), (b) 188 K (− 85 °C), (c) 173 K (− 100 °C), and (d) 77 K (− 196 °C).
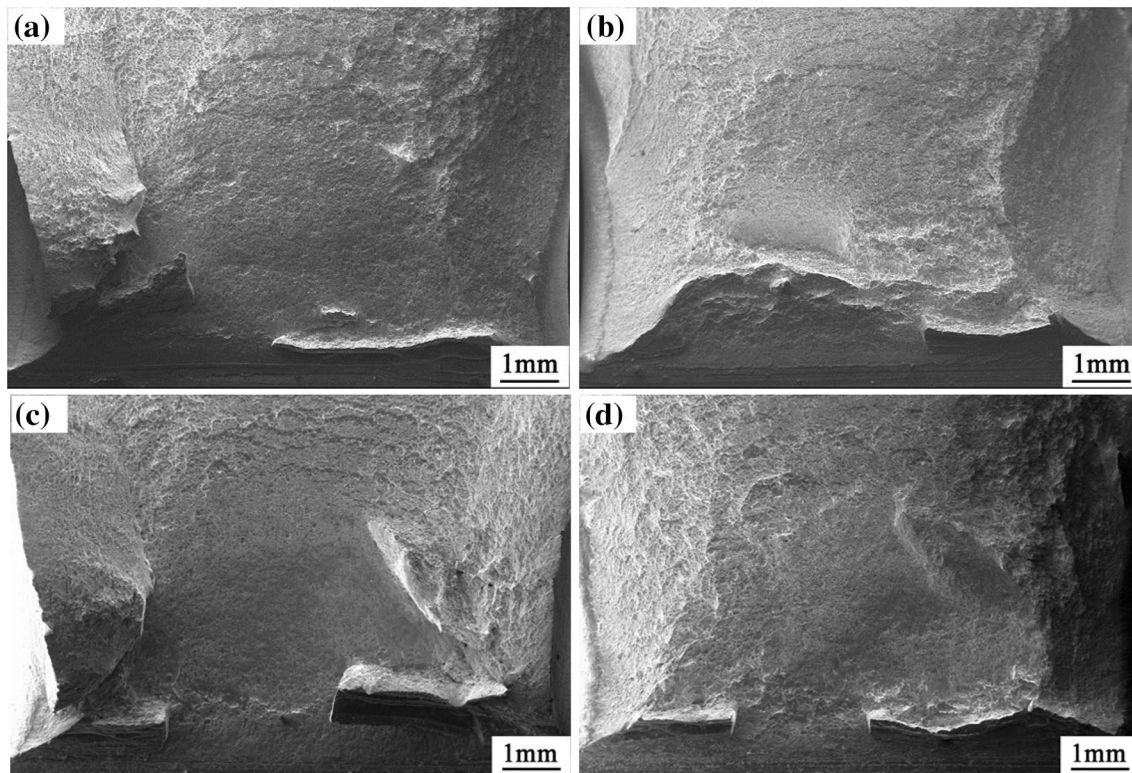
Fig. 15—SEM morphologies showing the fracture surfaces of Charpy V specimens austenitized at (*a*), (*b*) 1273 K (1000 °C), (*c*) 1473 K (1200 °C), (*d*) 1623 K (1350 °C) that failed at (a) 293 K (20 °C), (b) 188 K (−85 °C), and (c), (d) 293 K (20 °C).
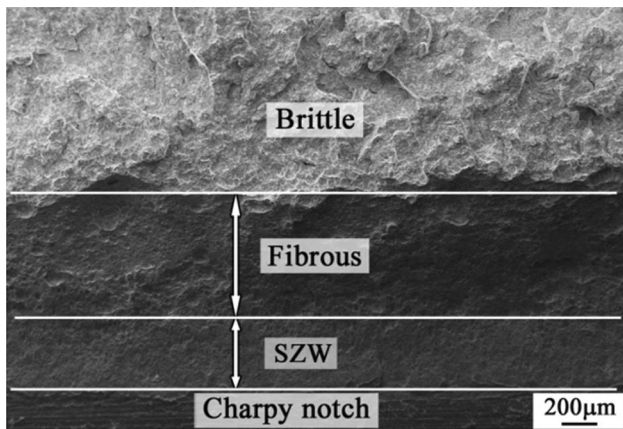

Fig. 16—SEM morphology showing the fracture surface of a Charpy V specimen austenitized at 1273 K (1000 °C) that failed at 153 K (− 120 °C).

identified as the propagation of the packet-sized crack in the high-strength steel.

G. *Estimated Brittle Fracture Stress σ_f*

The true local cleavage stress σ_f should be determined based on a test that results in brittle fracture with mitigated plastic deformation ahead of the notch. The microparameters achieved during the instrumented impact testing at 77 K (− 196 °C) are therefore suitable for determining the true σ_f. The brittle fracture load P_f prior to general yielding, the load at general yielding P_y, and σ_{dy} are given as follows. The values of P_f were directly measured (Figure 14(d)). The values of P_y at 77 K (− 196 °C) were determined by extrapolating the measured data at higher testing temperatures. Considering Figure 14 as an example, it is demonstrated how P_y was determined at higher testing temperatures from each curve of the instrumented Charpy V test. The σ_{dy} at 77 K (− 196 °C) was also extrapolated from those of higher temperatures calculated according to equation 4 (listed in Table III). Using the measured fracture load P_f and the calculated yield load P_y, suitable distribution curves of the stress, strain, and stress triaxiality ahead of the notch at 77 K (−196 °C) were calculated using the finite element method (FEM).

The FEM-based modeling of the Charpy V specimen was performed using the ABAQUS/Explicit code. A three-dimensional model with eight-node biquadratic plane-strain-reduced integration elements (C3D8R) of the ABAQUS code was used to calculate the normal stress (σ_{yy}) distribution in the Charpy V specimen with a notch root of 0.25 mm. Six-node linear triangular prism elements (C3D6) were used for the transition region. The boundary conditions are similar to the test conditions. For two bottom supporting blocks, the x, y, z displacements and rotational degrees of freedom (DOFs) were fixed. For the top loading block, at the initial step, the 6 DOFs were fixed, but at the loading analysis step, only the y-displacement DOF was released. The FEM mesh that was used is given in Figure 20.
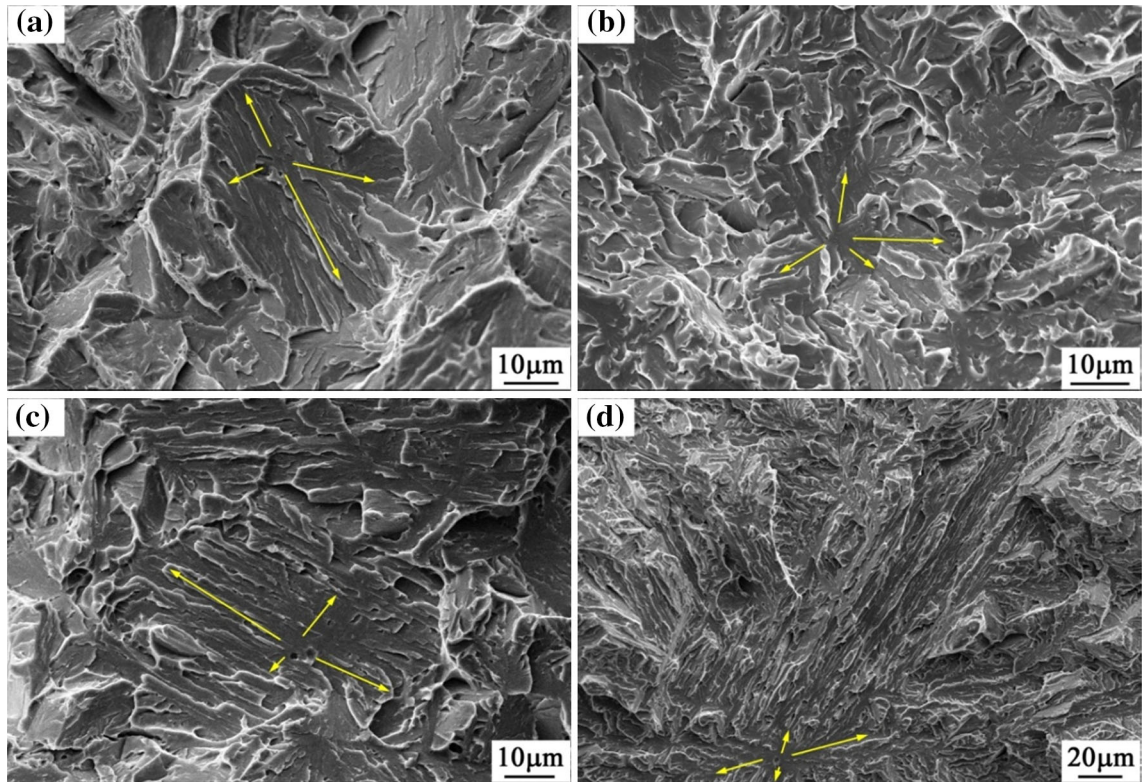
Fig. 17—SEM morphology showing the fracture surface near the crack-initiation site of a Charpy V specimen austenitized at (a) 1168 K (895 °C), (b) 1273 K (1000 °C), (c) 1473 K (1200 °C), and (d) 1623 K (1350 °C); all the samples failed at 77 K (− 196 °C).

The results of the FEM-based modeling are displayed in Figure 21. Plotting the fracture distance X_f on the abscissa and drawing a vertical line at the appropriate X_f value, the corresponding values of the ordinates on the curves of stress, strain, and stress triaxiality are determined as the local cleavage fracture stress σ_f, fracture strain ε_{pc}, and critical stress triaxiality T_c, respectively. The values of the microparameters are listed in Table III.

A comparison between σ_f and the variation in σ_{dy} vs temperature is plotted in Figure 22. The dynamic yield stress (σ_{dy}) changes with temperature. The σ_f determined at 77 K (− 196 °C) is also imposed in the figure and is assumed to be insensitive to temperature, based on previous studies.[1–3,40] Note that σ_{dy} would be intensified due to the geometric constraints to have the same meaning as the yield stress σ_Y indicated in the Yoffee diagram.[1–3] From the measured σ_f and the size of the cleavage facet area around the crack-initiation site a_f, the effective surface energy γ_p can be calculated by the following formula[2,5]:

$$\sigma_f = \sqrt{\pi E \gamma_p \big/ \left(1 - v^2\right) a_f} \quad \text{(for a penny − shaped crack)},$$

[5]

where E is Young's modulus, 200000 MPa, and v is Poisson's ratio, 0.3. The calculated values of γ_p and a_f are also listed in Table III.

The sizes of the cleavage facets change in the order consistent with the order of packet sizes, as shown in Figure 9. The packet sizes for the specimens austenitized at 1168 K and 1273 K (895 °C and 1000 °C) are similar, being the smallest. It is worth paying attention to the fact that the γ_f in the latter is substantially higher than that in the former. This can be attributed to the evolution of the microstructure from GB to LB, as shown in Figures 5 through 7.

IV. DISCUSSION

A. Effect of Austenitizing Temperature on Microstructural Evolution

The CCT behavior and microstructural evolution upon continuous cooling of the test steel austenitized at 1168 K (895 °C) have been investigated previously.[23] The current study extended the research by taking into account the effect of austenitizing temperature (or austenite grain size) on the microstructural evolution during the continuous cooling process. The cooling process should be comparable to that experienced by the core of the plates in industrial quenching when the thickness of the plates is 80 mm or greater.[23,25] The resultant microstructural factors changed upon increasing the austenitizing temperature over a wide range: the growth of prior austenite grains (Figure 1), reduced fraction of MA constituents from GB to LB/LM (Figures 6 and 7), increase in

Table IV. Microparameters for Fracture in the Ductile-to-Brittle Transition Region

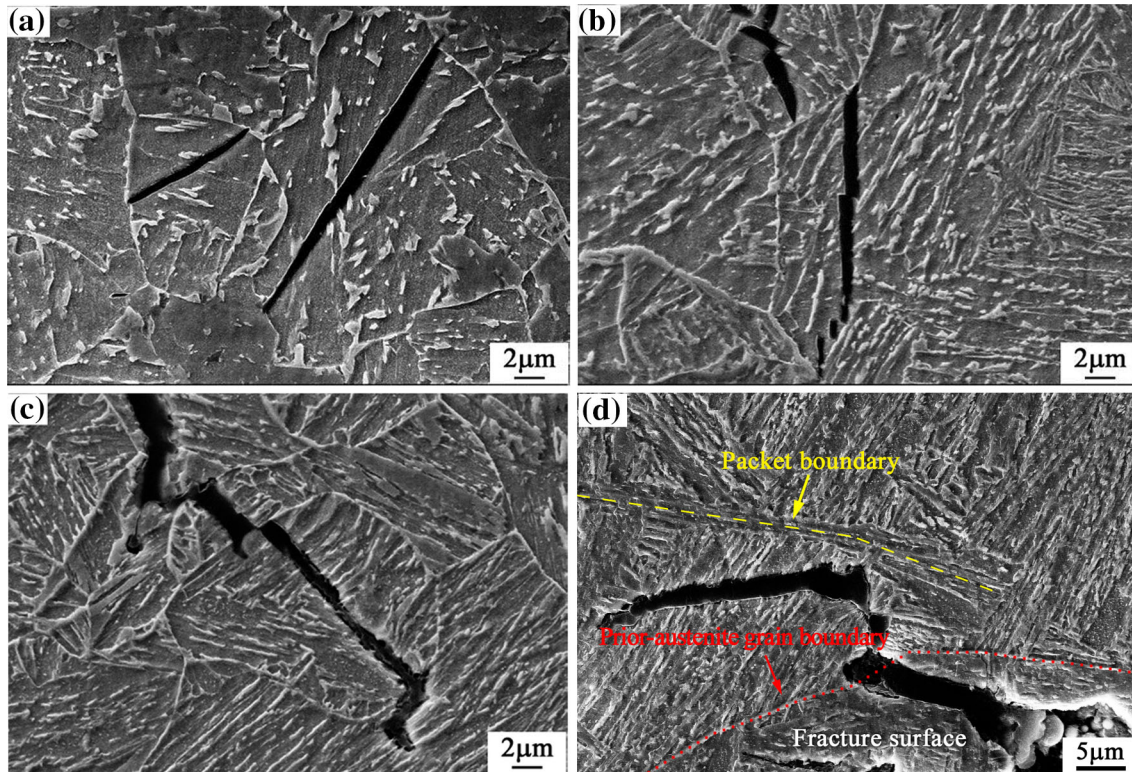| T_{RH} K (°C)	Test Temp. K (°C)	E_t (J)	SZW (μm)	SCL (μm)	SZW + SCL (μm)
1168 (895)	213 (− 60)	199	201	2497	2698
1273 (1000)	173 (− 100)	67	471	872	1343
1473 (1200)	188 (− 85)	35	108	323	431
1273 (1000)	153 (− 120)	65	410	806	1216

Fig. 18—Packet-sized crack retained in the specimen (*a*) austenitized at 1168 K (895 °C) and fractured at 188 K (− 85 °C), (*b*) austenitized at 1168 K (895 °C) and fractured at 77 K (− 196 °C), (*c*) austenitized at 1273 K (1000 °C) and fractured at 77 K (− 196 °C), and (*d*) austenitized at 1473 K (1200 °C) and fractured at 77 K (− 196 °C).

bainitic/martensitic packet size (Figure 9), or increased density of HAGBs (Figures 11 and 12). During the CCT, grain-boundary nucleation was observed to be the main mechanism at the start of the phase transformation. The coarse austenite grains (austenitizing at 1473 K and 1623 K (1200 °C and 1350 °C)) were fragmented due to the impingements (Figures 3 and 4). It should be emphasized that the HAGBs detected included prior austenite grain boundaries, packet boundaries, and the interlath high-angle boundaries in the packets. A packet should be enclosed by the first two types of boundaries. According to the observation, the density of the packet boundaries in the specimen austenitized at 1623 K (1350 °C) should be much lower than that in the sample austenitized at 1273 K (1000 °C).

The microstructural change from GB to LM is attributed to the increased hardenability of austenite as the austenitizing temperature is increased. The increased hardenability of austenite due to the increase in austenitizing temperature may be attributed to the increased dissolution of the alloy elements and microalloying precipitates (*e.g.*, Nb(CN)) in austenite. The increase in PAGS also results in the increased hardenability of austenite. This is attributed to the reduced fraction of austenite grain boundaries in the specimen, which are believed to be the preferred nucleation sites during austenite-to-ferrite transformation. Isothermal austenitization at 1168 K (895 °C) would result in the complete dissolution of any Cu-containing precipitates that are present prior to reheating; however, it is speculated that niobium-carbonitride precipitates would remain undissolved based on the study of Spanos *et al.* on a HSLA-100 steel.[26] Comparing with the case where the specimen was austenitized at 1168 K (895 °C), the increased hardenability of the austenite in the specimen austenitized at 1273 K (1000 °C) can be mainly
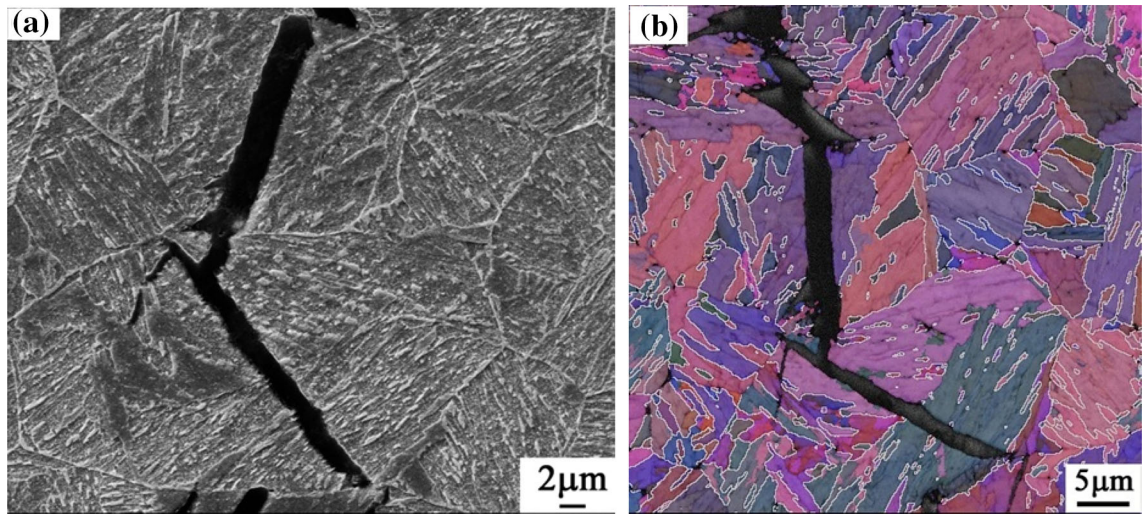
Fig. 19—SEM image of (*a*) retained cracks and (*b*) the corresponding EBSD (Euler angle color scheme) mapping for misorientations greater than 35 deg in the specimen austenitized at 1273 K (1000 °C) and fractured at 77 K (− 196 °C) showing the inhibition of the propagation of the cleavage by high-angle packet boundaries, rather than the HAGBs in the packets (Color figure online).
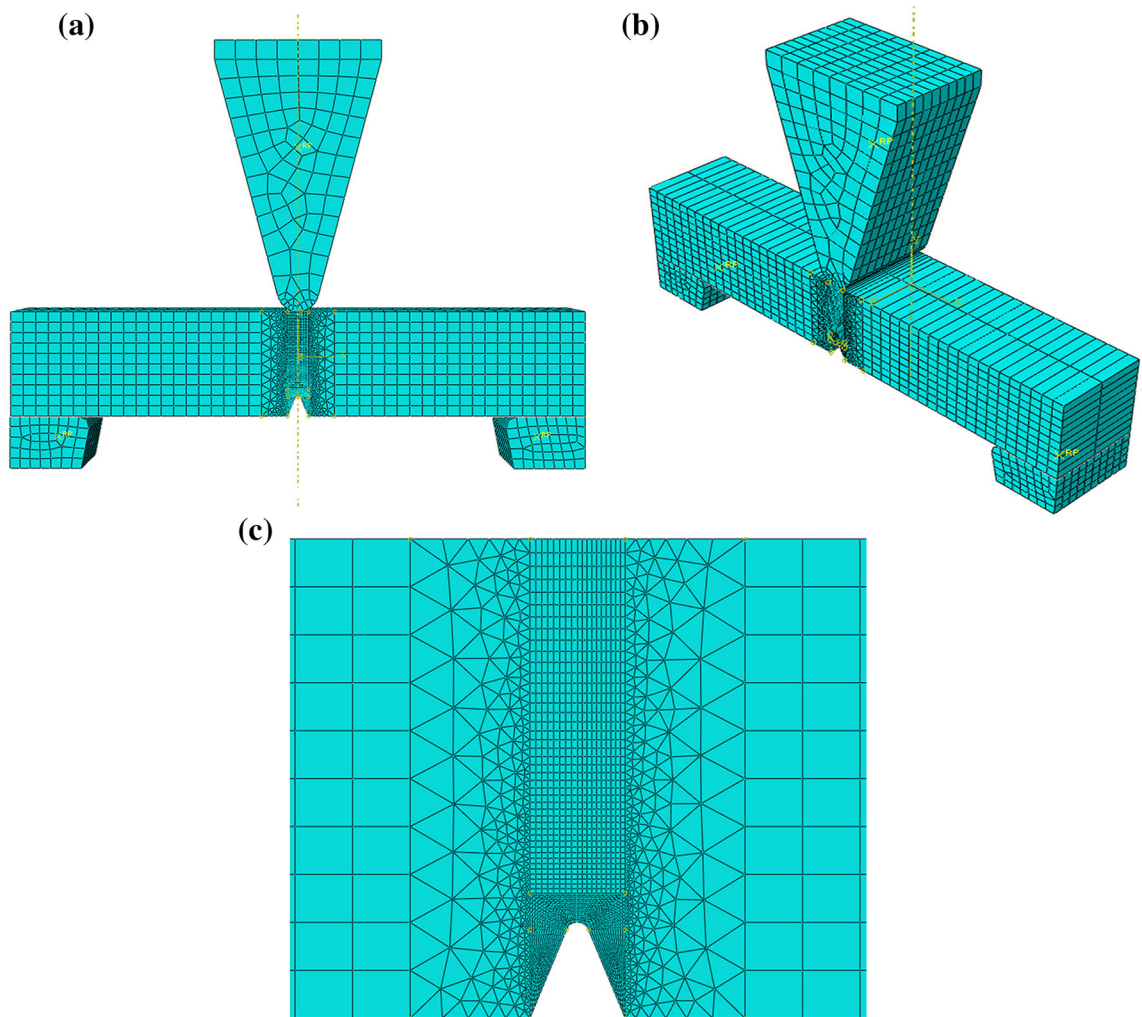

Fig. 20—Three-dimensional (3D) mesh arrangement for FEM-based calculation of a notched Charpy V specimen: (*a*) front view of the 3D model, (*b*) side view of the 3D model, and (*c*) magnified mesh distribution ahead of the notch root.
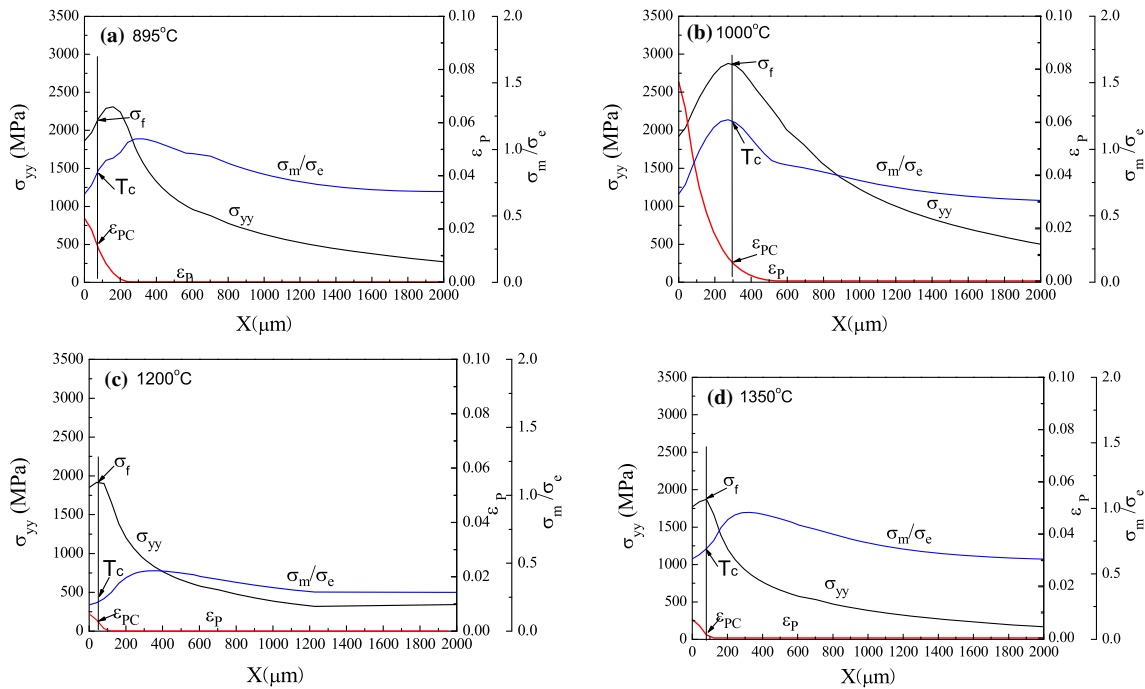
Fig. 21—Stress, strain, and stress triaxiality distributions ahead of the notch at fracture stress at 77 K (− 196 °C) for the specimens austenitized at (a) 1168 K (895 °C), (b) 1273 K (1000 °C), (c) 1473 K (1200 °C), and (d) 1623 K (1350 °C). The stress triaxiality T is a single non-dimensional parameter, which is defined as follows: $T = \sigma_m/\sigma_e$ for a specimen subjected to a triaxial state of stress, σ_1, σ_2 and σ_3, where σ_m is the mean or hydrostatic stress, being $(\sigma_1 + \sigma_2 + \sigma_3)/3$, and σ_e is the Von Mises equivalent stress (effective stress).
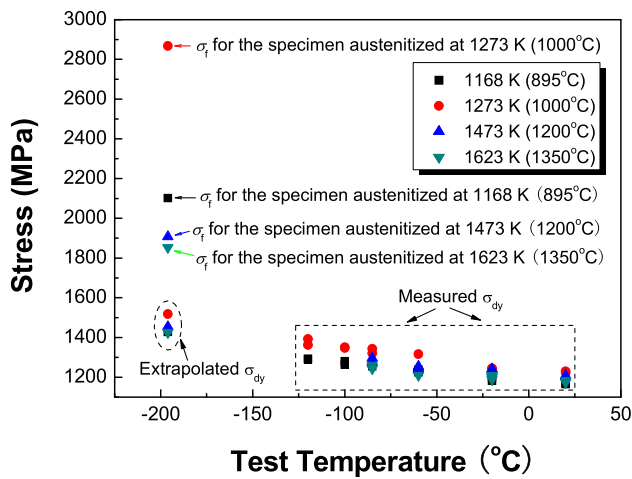

Fig. 22—Dynamic yield stress and identified fracture stress for the specimens austenitized at 1168 K, 1273 K, 1473 K, and 1623 K (895 °C, 1000 °C, 1200 °C, and 1350 °C)).

attributed to the increased dissolution of the alloy elements and increased austenite grain size. The temperature for substantial dissolution of the niobium-carbonitride precipitates varies with the content of Nb and thermal history. Shome *et al.*[41] calculated and confirmed that rapid dissolution of the precipitates takes place above 1441 K (1168 °C) for a simulated welding thermal cycle with a heat input of 10 kJ/cm and 1419 K (1146 °C) for 40 kJ/cm for a HSLA-100 steel with 0.029 wt pct Nb. For the thermal cycle employed in the present study, the temperature for the complete

dissolution of the niobium-carbonitride precipitates of the investigated steel should be 1397 K (1124 °C), according to Liu *et al.*[23,24] The substantial increase in the hardenability of the specimen austenitized at 1473 K (1200 °C) and higher can therefore be attributed to (1) a complete dissolution of the niobium-carbonitride precipitates, and (2) the substantial coarsening of the austenite grains, as shown in Figure 1.

B. *Microstructural Factors Affecting the Brittle Fracture Stress σ_f and Brittle Fracture Behavior*

According to the Griffith equation[5], σ_f is dependent upon (1) the size of the initial cleavage facet a_f, and (2) the effective surface energy γ_p of the cleavage fracture. The physical meaning of γ_p manifests itself as the resistance to crack propagation both inside the grains and through the boundaries.[5] Eq. [5] was in turn modified to the following equation[2,5]:

$$\sigma_f = \sqrt{\pi E \gamma_p / (1 - v^2) 2c} \qquad [6]$$

where $2c$ is the size of a newly initiated crack nucleus. Based on σ_f, the values of γ_p were calculated using the values of a_f in the current study. This was different from the methods reported in the literature. The average unit crack path (UCP) or packet size (d_{packet}) was used to replace $2c$ in calculating γ_p in the literature.[2,7,42] The ratio of UCP to d_{packet} is approximately 1.2 to 1.5 for bainitic and martensitic steels.[7] In the current study, the UCPs of each specimen fractured at 77 K (− 196 °C) have also been observed. An example is shown in
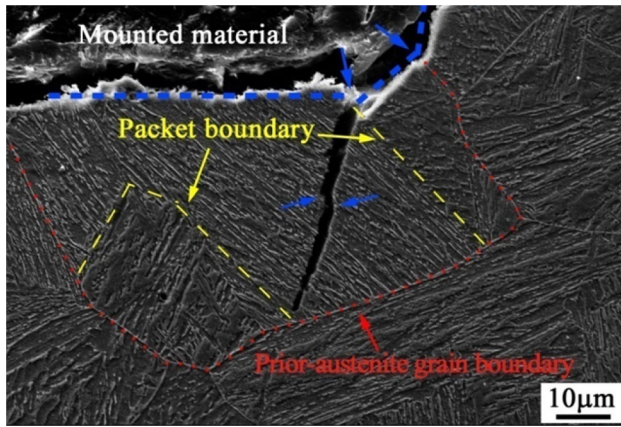
Fig. 23—SEM morphology of the cross-sectional area beneath the cleavage fracture surface of a Charpy specimen austenitized at 1623 K (1350 °C) and fractured at 77 K (− 196 °C) showing the crack-propagation path. The unit crack paths are outlined by the blue dashed lines. A retained crack propagation of which was deflected (indicated by blue arrows) and prevented by packet boundaries is also shown (Color figure online).

Fig. 24—Changes in σ_f, γ_p, and σ_{dy} with austenitizing temperature.

Figure 23 for the specimen austenitized at 1623 K (1350 °C). However, the authors believe that the true γ_p should be evaluated based on a_f, which better represents the real size of the initial crack nucleus.[6,8] Nevertheless, γ_p varies with the change in microstructural factors, which can be attributed to the increase in austenitizing temperature.

The HAGBs in the packet resist the propagation of the cracks in different ways, such as deflecting the crack paths and forming fine tear ridges on the fracture surfaces. The variation in the density of the fine tear ridges on the fracture surfaces (Figure 17) is consistent with the change in the density of the HAGBs detected by EBSD (Figure 11). The packet boundaries, however, play decisive roles by inhibiting or significantly deflecting the crack propagation (Figures 18, 19, and 23). The results of the current study are consistent with an early study by Naylor[43] that showed that major cleavage crack deviations occurred only at packet boundaries. The combined role of packet size and microstructural change determined the variation in fracture stress as follows. Although the bainite packet size in the specimen austenitized at 1168 K (895 °C) is the smallest, the value of the surface energy γ_p is also the smallest, due to the formation of GB with the lowest density of HAGBs. As a result, the fracture stress identified is not the largest. In the specimen austenitized at 1273 K (1000 °C), the bainite packet sizes increase slightly, whereas γ_p increases substantially. The fracture stress σ_f can therefore be maximized. In the case of the specimens austenitized at 1473 K or 1623 K (1200 °C or 1350 °C), the decreased fracture stress is mainly attributed to the coarsening of the microstructure. The variations in σ_f, γ_p, and σ_{dy} are plotted as functions of austenitizing temperature, as shown in Figure 24.

According to the Yoffee diagram, brittle fracture occurs when the yield stress σ_Y exceeds the cleavage fracture stress σ_f.[1–3] The DBTT changes from low-to high values in the order 179 K, 202 K, 217 K, and
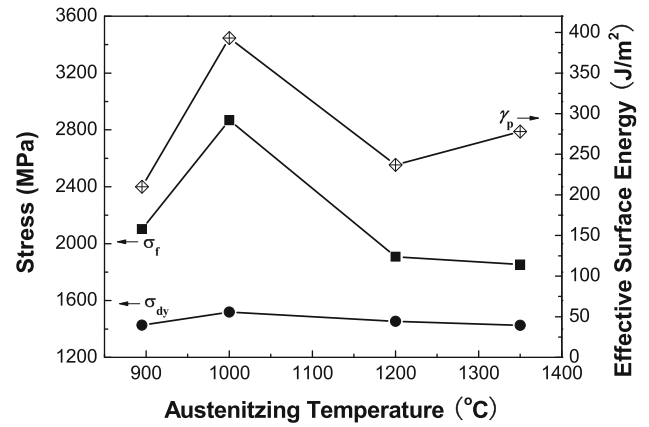
221 K (− 94 °C, − 71 °C, − 56 °C, and − 52 °C) (Table II), for σ_f values of 2868, 2102, 1908, and 1853 MPa (Table III), respectively. This variation in DBTT, associated with Figure 22, is in good agreement with the well-accepted concept indicated in the Yoffee diagram.[1–3] In the cases of impact loading on the V-notched specimens, the criterion for triggering a cleavage crack is expressed as

$$\sigma_{yy} \geq \sigma_f, \qquad [7]$$

where σ_{yy} is the normal stress ahead of the notch root, which is intensified from σ_{dy} through the equation $\sigma_{yy} = Q\sigma_{dy}$. During cleavage cracking, the stress intensification factor $Q = \sigma_{yy}/\sigma_{dy}$ evolves to the critical value $Q_c = \sigma_f/\sigma_{dy}$. The decrease in σ_f makes the cleavage fracture to occur more easily and increases the DBTT. It also causes early termination of the extension of the fibrous crack and reduces its length, thus decreasing the toughness in the transition temperature range.[5,8]

V. CONCLUSION

The microstructural evolution and factors affecting the ductile-to-brittle fracture in V-notched impact specimens of the 690 MPa (high-strength) steel were comprehensively investigated and the following conclusions were drawn:

(1) An increase in austenitizing temperature results in an increase in prior austenite grain size and its hardenability. Grain-boundary nucleation is the main mechanism of phase transformation during continuous cooling. The coarsened prior austenite grains are fragmented due to impingement during the growth of ferrite laths of different orientations within the austenite grains. The resultant microstructures evolve from a mixture of GB and LB to a mixture of LB and LM as the isothermal austenitizing temperature increases. Packet size increases in the lath microstructures as the austenitizing temperature is increased. The density of HAGBs, on the other hand, also increases as the austenitizing temperature is

increased. This is attributed to the formation of high-misorientation interlath boundaries in the packets of the coarse-grained specimens (Figure 11).

(2) The ductile-to-brittle transition temperatures (DBTTs) of the specimens austenitized at 1168 K, 1273 K, 1473 K, or 1623 K (895 °C, 1000 °C, 1200 °C, or 1350 °C) are 202 K, 179 K, 217 K, and 221 K (-71 °C, -94 °C, -56 °C, and -52 °C), respectively. The critical event for cleavage fracture is identified as the propagation of the packet-sized crack. The local fracture stresses σ_f are determined as 2102, 2868, 1908, and 1853 MPa for the different specimens. The presence of granular bainite-associated coarse martensite–austenite (MA) constituents deteriorates the Charpy impact toughness in the specimen austenitized at 1168 K (895 °C). The highest σ_f or the lowest DBTT is therefore achieved in the specimen austenitized at 1273 K (1000 °C) with reduced MA fraction.

(3) The optimal low-temperature toughness is not achieved in the specimen with the highest fraction of HAGBs and largest packet sizes. This is attributed to the fact that the density of high-angle packet boundaries is low. The high-angle packet boundaries are decisive factors in enhancing σ_f and decreasing DBTT by preventing the propagation of the cleavage crack and resulting in thick ridges on the fracture surface. The high-angle interlath boundaries in the packets provide an additional but not decisive resistance against the crack propagation by deflecting the crack path or forming fine tear ridges on the fracture surface.

(4) The results obtained from the current study indicate that both reduction in MA constituents and refinement of packet size are prerequisites to decrease the DBTT of the bainitic/martensitic steel.

REFERENCES

1. J.W. Morris, Jr.: *Science*, 2008, vol. 320, pp. 1022–23.
2. T. Hanamura, F. Yin, and K. Nagai: *ISIJ Int.*, 2004, vol. 44, pp. 610–17.
3. J.W. Morris, Jr.: *ISIJ Int.*, 2011, vol. 51, pp. 1569–75.
4. S.Y. Shin, K.J. Woo, B. Hwang, S. Kim, and S. Lee: *Metall. Mater. Trans. A*, 2009, vol. 40A, pp. 867–76.
5. J.H. Chen and R. Cao: *Micromechanism of Cleavage Fracture of Metals: A Comprehensive Microphysical Model for Cleavage Cracking in Metals*, Elsevier, Oxford, 2014, pp. 7–239.
6. R. Cao, X.B. Zhang, Z. Wang, Y. Peng, W.S. Du, Z.L. Tian, and J.H. Chen: *Metall. Mater. Trans. A*, 2014, vol. 45A, pp. 815–34.
7. A. Di Schino and C. Guarnaschelli: *Mater. Lett.*, 2009, vol. 63, pp. 1968–72.
8. R. Cao, J. Li, D.S. Liu, J.Y. Ma, and J.H. Chen: *Metall. Mater. Trans. A*, 2015, vol. 46A, pp. 2999–3014.
9. N. Isasti, D. Jorge-Badiola, M.L. Taheri, and P. Uranga: *Metall. Mater. Trans. A*, 2014, vol. 45A, pp. 4972–82.
10. A.F. Gourgues, H.M. Flower, and T.C. Lindley: *Mater. Sci. Technol.*, 2000, vol. 16, pp. 26–40.
11. A. Lambert-Perlade, A.F. Gourgues, J. Besson, T. Sturel, and A. Pineau: *Metall. Mater. Trans. A*, 2004, vol. 35A, pp. 1039–53.
12. J.W. Morris, C.S. Lee, and Z. Guo: *ISIJ Int.*, 2003, vol. 43, pp. 410–19.
13. J.W. Morris, C. Kinney, K. Pytlewski, and Y. Adachi: *Sci. Technol. Adv. Mater.*, 2013, vol. 14, pp. 1–9.
14. M. Tsuboi, A. Shibata, D. Terada, and N. Tsuji: *Metall. Mater. Trans. A*, 2017, vol. 48A, pp. 3261–68.
15. B. Huang, C.G. Lee, and S.J. Kim: *Metall. Mater. Trans. A*, 2011, vol. 42A, pp. 717–28.
16. S. Pallaspuro, A. Kaijalainen, S. Mehtonen, J. Kömi, Z. Zhang, and D. Porter: *Mater. Sci. Eng., A*, 2018, vol. 712, pp. 671–80.
17. A. Ghosh, S. Das, and S. Chatterjee: *Mater. Sci. Eng., A*, 2008, vol. 486, pp. 152–57.
18. S.K. Dhua, D. Mukerjee, and D.S. Sarma: *Metall. Mater. Trans. A*, 2003, vol. 34A, pp. 2493–2504.
19. S.K. Dhua, D. Mukerjee, and D.S. Sarma: *Metall. Mater. Trans. A*, 2001, vol. 32A, pp. 2259–70.
20. S.K. Dhua, A. Ray, and D.S. Sarma: *Mater. Sci. Eng., A*, 2001, vol. 318, pp. 197–210.
21. P.K. Ray, R.I. Ganguly, and A.K. Panda: *Mater. Sci. Eng., A*, 2003, vol. 346, pp. 122–31.
22. Y. You, X.M. Wang, and C.J. Shang: *Acta Metall. Sin.*, 2012, vol. 48, pp. 1290–98.
23. D.S. Liu, B.G. Cheng, and Y.Y. Cheng: *Metall. Mater. Trans. A*, 2013, vol. 44A, pp. 440–55.
24. B.G. Cheng, M. Luo, and D.S. Liu: *Ironmak. Steelmak.*, 2015, vol. 42, pp. 608–17.
25. D.S. Liu, B.G. Cheng, and Y.Y. Cheng: *Acta Metall. Sin.*, 2012, vol. 48, pp. 334–42.
26. G. Spanos, R.W. Fonda, R.A. Vandermeer, and A. Matuszeski: *Metall. Mater. Trans. A*, 1995, vol. 26A, pp. 3277–93.
27. M. Shome and O.N. Mohanty: *Metall. Mater. Trans. A*, 2006, vol. 37A, pp. 2159–69.
28. D. Chae, C.J. Young, D.M. Goto, and D.A. Koss: *Metall. Mater. Trans. A*, 2001, vol. 32A, pp. 2229–37.
29. S.K. Dhua, D. Mukerjee, and D.S. Sarma: *ISIJ Int.*, 2002, vol. 42, pp. 290–98.
30. K. Banerjee and U.K. Chatterjee: *Metall. Mater. Trans. A*, 2003, vol. 34A, pp. 1297–1309.
31. K. Banerjee, M. Militzer, M. Perez, and X. Wang: *Metall. Mater. Trans. A*, 2010, vol. 41A, pp. 3161–72.
32. D.S. Liu, Q.L. Li, and T. Emi: *Metall. Mater. Trans. A*, 2011, vol. 42A, pp. 1349–61.
33. W.L. Server: *J. Eng. Mater. Technol.*, 1978, vol. 100, pp. 183–88.
34. X.F. Zhang, P. Han, H. Terasaki, M. Sato, and Y. Komizo: *J. Mater. Sci. Technol.*, 2012, vol. 28, pp. 241–48.
35. H. Terasaki and Y.I. Komizo: *Metall. Mater. Trans. A*, 2013, vol. 44A, pp. 2683–89.
36. G. Mao, R. Cao, X. Guo, Y. Jiang, and J.H. Chen: *Metall. Mater. Trans. A*, 2017, vol. 48A, pp. 5783–98.
37. E.I. Galindo-Nava and P.E.J. Rivera-Diaz-del-Castillo: *Acta Mater.*, 2015, vol. 98, pp. 81–93.
38. S.W. Thompson, D.J. Colvin, and G. Krauss: *Metall. Mater. Trans. A*, 1996, vol. 27A, pp. 1557–71.
39. S.Y. Sung, S.S. Sohn, S.Y. Shin, K.S. Oh, and S. Lee: *Metall. Mater. Trans. A*, 2014, vol. 45A, pp. 3036–50.
40. J.H. Chen, L. Zhu, and H. Ma: *Acta Metall. Mater.*, 1990, vol. 38, pp. 2527–35.
41. M. Shome, D.S. Sarma, O.P. Gupta, and O.N. Mohanty: *ISIJ Int.*, 2003, vol. 43, pp. 1431–37.
42. L. Rancel, M. Gómez, S.F. Medina, and I. Gutierrez: *Mater. Sci. Eng., A*, 2011, vol. 530, pp. 21–27.
43. J.P. Naylor: *Metall. Trans. A*, 1979, vol. 10, pp. 861–73.